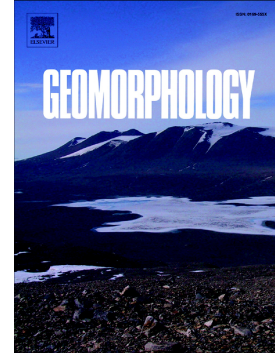# Journal Pre-proof

Exploring event landslide mapping using Sentinel-1 SAR backscatter products

Michele Santangelo, Mauro Cardinali, Francesco Bucci, Federica Fiorucci, Alessandro Mondini

Please cite this article as: M. Santangelo, M. Cardinali, F. Bucci, et al., Exploring event landslide mapping using Sentinel-1 SAR backscatter products, *Geomorphology* (2021), https://doi.org/10.1016/j.geomorph.2021.108021

This is a PDF file of an article that has undergone enhancements after acceptance, such as the addition of a cover page and metadata, and formatting for readability, but it is not yet the definitive version of record. This version will undergo additional copyediting, typesetting and review before it is published in its final form, but we are providing this version to give early visibility of the article. Please note that, during the production process, errors may be discovered which could affect the content, and all legal disclaimers that apply to the journal pertain.

Exploring event landslide mapping using Sentinel-1 SAR backscatter products

Michele Santangelo* (1), Mauro Cardinali (1), Francesco Bucci (1), Federica Fiorucci (1), Alessandro Mondini (1)

(1) CNR-IRPI, Via Madonna Alta, 126, Perugia.

*Correspondence to: michele.santangelo@irpi.cnr.it

Abstract

Landslides triggered by meteorological phenomena occur worldwide and cause extensive and severe damages to properties, and life loss. Detailed maps of event landslides can sensibly shorten emergency response time, possibly resulting in reduced death tolls. In most cases, however, optical post-event images are not always available right after the event, due to dense cloud cover. Since Synthetic Aperture Radar (SAR) sensors overcome the limitation of cloud cover, in this work we explore the use of C-band Sentinel-1 SAR amplitude images to map event landslides. A team of four expert photo-interpreters first defined interpretation criteria of SAR amplitude post-event images of the backscatter coefficient (β_0) and of the derived images of change. The same team mapped two large event landslides occurred in Villa Santa Lucia (Chile) and Tonzang (Myanmar). Maps were prepared on a total of 72 images for the Chile test case and 54 for the Myanmar test case. Images included VV (vertical transmit, vertical receive) and VH (vertical transmit, horizontal receive) polarisation, ascending and descending orbits, multilook processing, adaptive and moving window filters, post-event images and images of change. In the first case, interpreters were asked to map the event landslide on an optical post-event image before mapping on SAR images, whereas in Myanmar it was done in the end. Results were quantitatively compared to the maps prepared on post-event optical images, assumed as benchmark. Results revealed a good agreement between the SAR-derived maps and the benchmark. Locally, errors can be due to geometrical distortions, and speckling-like effects. Also polarisation plays an important role, as opposed to filtering. Despite the preliminary nature of this study, it proved that SAR amplitude derived products are suitable to prepare accurate maps of large event landslides, and that they should be further tested to prepare event inventories.

Keywords

Event landslides; landslide detection; landslide mapping; Sentinel-1; Synthetic Aperture Radar amplitude; Disaster fast response

1 Introduction

Landslides can be triggered by natural phenomena such as intense and prolonged rainfall (*Ardizzone et al., 2012*), earthquakes (*Santangelo et al., 2019*), rapid snow/ice melting (*Duhart et al., 2019*), volcanic eruptions (*Francis, 1993*), but also by anthropic activities such as mining,

quarrying, road building (*Jaboyedoff et al., 2016*). Landslides are complex physical processes that can involve different types of movement depending on lithology, trigger, water content (among the main factors). When landslides occur, they leave discernible features on the landscape. The ensemble of the features (morphologic and radiometric) that are left by landslides is usually referred to as "landslide signature" (*Fiorucci et al., 2018; Niculiţă et al., 2016*). The morphologic and radiometric signatures are exploited by geomorphologists to detect, map and classify landslides, both in the field and on remotely sensed imagery (*Guzzetti et al., 2012*). Depending on the considered band of the electromagnetic spectrum, the portion of the landslide signature portrayed in the images can be (even sensibly) different.

Landslides that can be related to a specific triggering event are referred to as event landslides (*Guzzetti et al., 2012*). Landslides of different types and magnitudes can show different radiometric signatures, also depending on the type and intensity of the event. For example, slow-moving shallow soil slides change very little of the land cover, and are better visible on stereoscopic images compared to monoscopic optical images (*Fiorucci et al., 2011*). On the contrary, fast moving earth flows or debris flows cause large changes in the land cover, and can be easily detected in monoscopic optical images by interpreters (*Fiorucci et al., 2018*) or even through change detection algorithms (*Guzzetti et al., 2012, Mondini et al., 2012*). The landslide morphological signature is an expression of the type of movement, and is the feature that most of all allows interpreters to classify landslides. Of course, deep-seated landslides usually show a more pronounced morphological signature than shallow landslides. In general, depending on the type of event, and on the type of movement and magnitude of triggered landslides, remote sensing images in different ranges of the electromagnetic spectrum, of different types and at different resolutions can be more or less suitable for landslide detection and mapping compared to others, and even be completely "blind" in some cases.

The most important criterion that geomorphologists and image interpreters adopt for detecting landslide signatures in a landscape is that landslides appear as local anomalies in the general continuity of other features. Generally, small landslides (10^2-10^4 m^2) tend to represent anomalies in local land cover (e.g., interruption of vegetation), landslides larger than 10^4 m^2 tend to represent also anomalies of the local morphology (e.g. interruption of the lateral continuity of scarps), kilometre-scale landslides may include also anomalies in the local geology (e.g., interruption of continuity of geological formations).

For most events triggered by meteorological phenomena, remote sensing within the optical range suffers from limitations due to cloud coverage (*Plank et al., 2016; Mondini et al., 2019*) in the immediate aftermath of the event. This is why growing research efforts are exploring the capabilities of the all-weather Synthetic Aperture Radar (SAR) systems to capture evidence that may allow geomorphologists to identify and possibly map landslide events, worldwide (*Mondini et al., 2019*), and in presence of clouds (*Plank et al., 2016; Mondini et al., 2019*).

SAR systems illuminate the ground with an electromagnetic wave in the microwave spectral range, and record the amplitude and the phase of the backscattered signal.

SAR amplitude derived products, including intensity and some derived backscatter coefficients, have been used to identify and map landslides with a photo-interpretative approach since 1995 (*Singhroy, 1995; Vargas Cuervo, 1997; Chorowicz et al., 1998; Singhroy et al., 1998; Mondini et al., 2019;*), and only recently with quantitative methods (*Mondini, 2017; Konishi and Suga, 2018a, 2018b; Ge et al., 2019; Uemoto et al., 2019*).

Singhroy, (1995) complemented traditional methods used for landslide inventories in the Lower

Fraser Valley, Canada, through a description of the landslide features (i.e. slide scars, rupture line, debris lobe), in 6-m resolution C-HH-band, airborne SAR images in combination with Landsat Thematic Mapper (TM) optical images. Information on how the image portrays landslide features is given when the author describes the debris lobe as appearing in light tones. They claimed, however, characterisation and mapping require high resolution imagery, particularly referring to SAR data.

Singhroy et al. (1998) repeated the experiment in the Lower Fraser Valley, Canada, using a number of 18 m – 26 m (Range) x 27 m (Azimuth) resolution C-band spaceborne RADARSAT SAR images with different viewing geometry. They concluded that RADARSAT incidence angles ranging from 40 to 59 degrees were suitable to map block slide scarps and transverse ridges, associated with rock slumps and faults. They recommend the high resolution fine mode image.

Cuervo, (1997) used C-band spaceborne ERS-1 stereo-simulated images to map seven landslides in Columbia at a scale of, approximately, 1:50.000. The capability of SAR images to emphasise landslide features is related to the presence of different tones in the surrounding of the landslide: where the ground is smooth the tones are dark; inside the landslide the rough(ness) surface has light tones due to high values of surface backscatter.

Also *Chorowicz et al. (1998)* showed the efficacy of geomorphological landslide mapping of stereo-simulated airborne 12 m resolution C-band ERS-1 or 18 m resolution L-band JERS-1 images, in Chicamocha valley, Colombia. They described geomorphological features on the stereo images as changes in backscatter, and highlighting the limitation of landslide recognition due to landslide size and layover. The geomorphic features recognised in the interpretation are scarps, convex or concave slopes, horizontally curved steps, and irregularities in stream alignments. Those features are detected as anomalies in their context. Despite their lower spatial resolution, JERS-1 images were preferred to ERS-1 images due to their more favourable angle of view for the preparation of the virtual stereo-couple.

Furuta and Tomiyama (2008) used the Normalised Sigma-Naught Index NDSI derived from spaceborne L-band ALOS SAR images for the identification of a large rock slide triggered by a 6.4 Mw earthquake occurred in Pakistan, Ziarat, the 29th of October, 2008.

After more than ten years, *Mondini et al. (2019)* presented a systematic analysis to assess the possibility to detect landslides using measures of change of the backscatter coefficient between couples of spaceborne C-band Sentinel-1 SAR images. The dimensionless surface radar backscatter coefficient, β_0, also called radar brightness coefficient is the Radar Cross Section (RCS) per unit area in the radar's line-of-sight for distributed targets. Compared to σ_0 (i.e. sigma naught, the backscatter coefficient), the RCS per unit area in the ground range, the local incidence angle of the radar signal has no impact on β_0, which is, hence, less sensitive to the approximations in the local incidence angle estimation (*El-Darymli et al., 2014*). In their study, 32 single or multiple landslide events, different in type, size, topographic aspect, process and geographical, geological, and geomorphological settings, were detected thanks to the analysis of variables such as the spatial patterns of β_0 changes, caused by the landslide occurrence.

Despite the scientific advancements in the use of SAR amplitude derived products, a detailed and

quantitative analysis of the suitability of these images for landslide visual interpretation is lacking, and little effort has been done to establish and describe the criteria used for image interpretation, and their connection with the physical parameters recorded in the SAR satellite images.

Recently, some authors have started to use SAR amplitude derived products for rapid mapping of landslides using machine learning approaches (*Suga and Konishi, 2012; Mondini, 2017; Konishi and Suga, 2018a; Ge et al., 2019; Uemoto et al., 2019; Adriano et al., 2020; Esposito et al., 2020*). Short revisiting time (6 days for Sentinel-1 at middle latitudes, *The European Space Agency, 2021a*), free availability, and global coverage make SAR amplitude products suitable to prepare near-real time landslide event inventories on a global scale. Encouraged by the unprecedented availability of SAR imagery and the growing interest within the scientific community (*Mondini et al., 2021*), in this work we attempt to (i) formalise criteria used to map two event landslides chosen as test cases through heuristic interpretation of SAR images, (ii) measure their informative content, and (iii) understand their limitations and potential for event landslide mapping, limited to Sentinel-1 C-band SAR amplitude derived products.

In this paper, we use the word "image" when referring both to the original images acquired by the sensors and to the derived images obtained after pre-processing steps. The expression "derived image" and "derived products" are used as synonyms and refer only to images obtained from the original images through pre-processing steps.

The paper follows this structure: Section 2 describes SAR amplitude images, the pre-processing, and the criteria defined for heuristic interpretation of event landslides. Section 3 presents the experiment designed to measure the informative content of the SAR images and to define the usability of such images for event landslide mapping. Section 4 presents the two case studies and the images available for carrying out the experiment. Section 5 presents the results, while in Section 6 a discussion deals with limitations of this study, its applicability and illustrates future work. Section 7 summarises the conclusions.

2 Framework

2.1 SAR images

The two Sentinel-1 Synthetic Aperture Radar (SAR) satellites are active systems operating in the microwave spectral range. The right side looking Sentinel-1 SAR antenna sends a C-band signal with a central frequency of 5.4 GHz (corresponding to a wavelength λ of about 5.5 cm) and records the strength of the back scattered echo, and the time to return. Amplitude and phase of the echo are stored in the real in-phase component (I) and imaginary quadrature component (Q).

The instrument can operate in single (horizontal transmit horizontal receive, HH, vertical transmit vertical receive, VV), or in dual polarisation (horizontal transmit horizontal receive and horizontal transmit vertical receive HH+HV, vertical transmit vertical receive and vertical transmit horizontal receive, VV+VH), and in multiple acquisition modes. The default acquisition mode over land is the Interferometric Wide swath (IW), in which a good compromise between a large swath width (250 km) and a moderate geometric resolution (5 m × 20 m) is achieved (*The European Space Agency, 2021a*).

The images can be downloaded for free from the Copernicus Open Access Hub (*Copernicus Open Access Hub, 2021*) maintained by the Copernicus programme. Level-1 data are the products intended for most data users, and they can be in Single Look Complex (SLC) or in Ground Range Detected (GRD). Both are focused SAR data, the former in SAR geometry, the latter multi-looked and projected to ground range using an Earth ellipsoid model. SLC images can be calibrated through Look Up Tables (LUT) to obtain β_0 the Radar Cross Section per unit area in the radar's line-of-sight (*El-Darymli et al., 2014*). Calibration makes it possible to extract geophysical parameters from the images and to compare images acquired in different times or from different sensors (*Freeman, 1992; Oliver and Quegan, 2004*). β_0 is mainly influenced by the surface parameters including roughness, geometric shape and dielectric properties of the target, and it is a function of the radar observation parameters including frequency, polarisation, and incidence angle, or its component along the range plane (the plane formed by the satellite, target and Earth centre), the projected local incidence angle (PLIA), and it can then be used to get information about the imaged surface.

Two factors can mainly hinder the use of SAR images: the side looking acquisition geometry and the speckling-like noise presence. The side looking configuration brings to represent the pixel coordinates in sensor geometry, in which the coordinates are the distance from the radar track (range) and direction of travel (azimuth), with the spatial resolution changing in relation to radar track distance. The original images are then not superimposable to images in ground coordinates. Furthermore, geometric distortions including foreshortening, layover, and shadow occur particularly in mountainous areas, where landslides are likely to occur. Foreshortening can be mitigated through geometric transformations, while layover and shadows can only be estimated, masked, or taken into account during the classification processes.

In the amplitude and in the amplitude derived products, the noise can be high and disturbing. It can be explained by the presence of many and different small scatters in every pixel illuminated by the beam *(Oliver and Quegan, 2004)*. The noise is usually modelled as a multiplicative component of the Radar Cross Section and the problem can be mitigated using SAR specific filters (*Frost et al., 1982; Lee et al., 1994; Vasile et al., 2006*).

Level-1 Interferometric Wide (IW) Single Look Complex (SLC) Sentinel-1 were used. Images are in slant range by azimuth imaging plane, in the image plane of satellite data acquisition. Each polarisation channel contains both amplitude and phase information (*The European Space Agency, 2021b*). All the pre-processing steps were performed using the SNAP - ESA Sentinel Application Platform version 7.0 (*STEP - Scientific Toolbox Exploitation Platform, 2021*).

Images were prepared for the interpretation with different levels of pre-processing. The first level included a thermal noise correction (*The European Space Agency, 2021c*), a calibration to obtain the surface radar backscatter coefficient β_0 *(El-Darymli et al., 2014; The European Space Agency, 2021d)* for each polarisation channel, a refinement of the orbit state vectors and deburst process to re-sample to a common spacing grid in range and azimuth. A second level of pre-processing consisted of a multi-looking process with a number of four and one looks respectively for the range and azimuth directions to obtain square pixels of about 14.3 m. The multi-looking process also reduces the speckling-like presence in the SAR images. To obtain the fourth level of pre-processing, images were further filtered using the Frost filter (*Frost et al., 1982*) or the Intensity-Driven Adaptive-Neighborhood (IDAN) filter (*Vasile et al., 2006*). The first obtains local estimates in adaptive neighbourhoods using regular moving windows, the last in regions previously defined through region growing processes. The IDAN filter should result in

a more smoothed signal in homogeneous areas, while the Frost in a better preservation of the big discontinuities in the signal. Processing parameters were respectively filter size (X,Y) = (3,3) and Damping Factor = 3 for the Frost filter and Number of looks = 1 and Adaptive Neighbour Size = 50 for the IDAN filter. The fifth and last pre-processing level was devoted to measuring the backscatter coefficient changes eventually occurred between the pre- and the post-event image. It included a DEM assisted co-registration between any couple of pre- and post-event single channel polarisation images using the SRTM 1 Sec HTG DEM (*Earth Resources Observation And Science (EROS) Center, 2017*), Nearest Neighbour post-event resampling, and a natural logarithm of the ratio between the just co-registered post- and pre-event single channel polarisation images (i.e., $ln(\beta_0 post_{VV}/\beta_0 pre_{VV})$). Among the several ways to estimate parameter changes between two acquisitions, we chose to compute the ratio of the two images. The logarithm helps to reduce the dynamic range in particular when the backscatter is low (close to zero) in the pre-event image, and it increases in the post-event image.

The products obtained from the different pre-processing levels were all orthorectified in geographic coordinates using a Range-Doppler method *(Small and Schubert, 2008)*, the SRTM 1 Sec HTG DEM and resampling methods. The tool applied through the SNAP - ESA Sentinel Application Platform is referred to as Terrain Correction. Shadowed and in layover areas were also simulated using the same SRTM 1 Sec HTG DEM.

2.2 Interpretation of SAR amplitude derived products

In the literature, image interpretation is generally based on a reproducible and rigorous set of rules, which is built on a four-stages process (*Ray, 1960; van Zuidam, 1986*): (i) reading, (ii) identification, (iii) classification, (iv) deduction. The first stage requires that the image is read to identify the general grain (fine or coarse), pattern (e.g., elongated, curved, straight), tone (generally dark or light, with clusters), texture (dotted, parallel, mottled). The second stage involves identification of objects, without classifying them. Identification means that within the general pattern of the image, the interpreter can discern that clusters of pixels tend to align along a given direction and cluster according to a shape, define a regular or irregular pattern, are consistently characterised by a grey tone, or by bands of alternating grey tones. Once identification takes place it is possible to apply a classification scheme which assigns a name to all the identified objects, usually according to a legend. This step involves the ability to make associations between image objects and the real world. The last step includes deduction, and involves making inferences on the processes underlying the objects already classified.

Geomorphologists use the classified objects in the images to detect anomalies. For instance, if the interpreter has identified a linear element that is classified as the surface evidence of bedding, its sudden interruption represents an alert that must be further investigated. Interpreters then use collateral elements to test the "landslide hypothesis". Such elements can be the shape of the grey tones clustering and its compatibility with the local morphological context, the pattern of the valley bottom, the interruption of other linear and continuous elements (roads or rivers or low order divides, boundaries between vegetated and bare areas). After the deduction process, the interpreter decides whether a given anomaly in the image is due to a landslide or not (i.e., converging evidences, *van Zuidam, 1986*), and eventually draws the polygon (mapping) that maximises the internal consistency of all the elements that refer to a single landslide. Interpretation of images remains a process strongly dependent on the interpreter's background

and experience, which is particularly true for classification and deduction steps.

In monoscopic optical images, event landslides are mapped through the portion of their radiometric signature which is in the visible wavelength range. In general, visual elements that are exploited by geomorphologists are represented by interruption of vegetation, of the lateral continuity of linear elements such as fields boundaries, infrastructures, regularity of river paths, of bedding traces, of local tectonic alignments. Slow-moving landslides often have a subtler fingerprint on the landscape, and can be recognised mainly through analysis of pattern and tone changes (*Fiorucci et al., 2011*). For example, disturbances in the pattern of cultivated fields, mottled shadows distribution can indicate areas with hummocky topography, and areas with lighter (or darker) colour tones indicate areas where soil moisture is lower (or higher). Also vegetation can show changes in colour due to landslide occurrence. When evidence is subtle, mapping event landslides can be carried out comparing pre- and post-event images.

SAR backscatter products are generally represented by a grey tone matrix of backscatter values mainly influenced by (i) the PLIA, (ii) surface roughness, and (iii) the dielectric constant, usually related to soil moisture (*Oliver and Quegan, 2004*). Landslides can be read in the grey tone matrix in terms of tone, texture, pattern, mottling and grain, and/or their changes, similarly to optical images. Event landslides cause changes in the backscatter pattern of an area, and appear as local anomalies. Therefore, we can refer to a "radar backscatter signature" of event landslides as the combination of these three main components which can reveal the occurrence of a landslide in radar amplitude products. Interpreters can tentatively learn how to discern, read and interpret such features to infer the presence of event landslides (landslide detection), and to delineate landslide borders (landslide mapping), similarly to what is done for optical post-event images.

The difference between the set of rules of the image interpretation process applied to optical images and the one applied to radar backscatter images lies in the different informative content of the pixels. In radar backscatter images, the interpretation process is based on the three elements stated above: orientation angle, surface roughness and dielectric constant as a proxy for soil moisture. Compared to optical images, interpretation of SAR images is partly limited by geometrical distortions, and speckling-like effects. Also, when passing from optical images to radar images, the degree of acquaintance with this type of image is reduced. Therefore, also the deductive process has to be based on a reduced set of elements and variables, which increases uncertainty and introduces mapping errors. To reduce a large part of the uncertainty, it is fundamental that pre-event and post-event images are examined jointly. It can help the interpreters spot the changes as areas where a landslide has occurred.

In general, the backscattering signal is higher (and the image appears whiter) when the PLIA is low, when the surface roughness is high (leaving polarisation and wavelength unchanged), and when the soil moisture is high. Water appears black. The PLIA mirrors the local morphology, since the darker and lighter tones cluster according to the local topographic aspect. When comparing pre- and post-event images, increasing water content or surface roughness causes an increase in the backscattering signal, as opposed to increasing PLIA. Likely, the change of the signal caused by a landslide is a combination of the 3 (and more) factors that can be estimated singularly only when ancillary data and inversion models are used. When the factors are competing, the ambiguities can be partially overcome by examining the context of the changes (e.g. interruption of the lateral continuity of other elements, the shape of the changes).

The interpretation process described for post-event images cannot be applied as is to LR images. Therefore, we define different criteria to interpret log ratio (LR) images, where clusters of pixels of changes pop out from the salt and pepper matrix (i.e. anomalies). Such changes can be caused by slope failures but also by snowmelt, rainfall, vegetation cuts, for example. Interpreters identify areas where the change has not been random, and decide whether the cluster is a landslide based on the shape of the cluster.

Finally, if necessary, to reduce uncertainty in the interpretation of any of the images described above, interpreters can use ancillary information such as Digital Elevation Models to drape the images and explore them in 2.5D images (similar to Google Earth™). Such an approach allows interpreters to exclude clusters that appear incompatible with the local morphology, as it could be in case of clusters elongated across the maximum slope direction.

2.3 Maps comparison

We have built an experiment based on two test cases to (i) measure the informative content of the SAR images used and (ii) understand the usability of SAR amplitude products for event landslide mapping. In the first case, mapping was carried out with a priori knowledge: interpreters mapped the landslide first on the optical post-event image and all available ancillary information. In the second case, no a priori information was used to map the landslide in the SAR images. In both cases, optical post-event maps were used as a benchmark.

The interpretation process was carried out by the same team of four expert photo-interpreters (FB, FF, MC, MS) who had also defined the interpretation criteria before mapping, through an iterative process using the a priori knowledge on the ground truth. The mapping was performed as a group to reduce subjectivity in the interpretation (*Guzzetti et al., 2012*). In both test cases, the task of the team was to draw the landslide border (*mapping*) on each image adopting the interpretation criteria. This operation was necessary to measure the information content of the SAR images against the benchmark. Assuming that our polygon summarises the information contained in the single image about that landslide, the deviation of each polygon from the benchmark can be attributed almost absolutely to the different information content, i.e. how much of the landslide radiometric signature is portrayed in that given image. This concept is the rationale for ranking the polygons and the corresponding images based on their comparison to the benchmark.

Comparison of maps to their benchmark was carried out in a pairwise fashion according to the error index (M_{Bi}) as in Equation 1 (*Carrara, 1993; Ardizzone et al., 2002; Santangelo et al., 2015; Fiorucci et al., 2018;*):

$$M_{Bi} = \frac{A_i \cup B_i - A_i \cap B_i}{A_i \cup B_i} \qquad (1)$$

where $A_i \cup B_i$ represents the area of the union of two landslide polygons, $A_i \cap B_i$ is the area of the intersection of the two landslide polygons. According to Equation 1, the mismatch (M_{Bi}) ranges between 0 and 1, where 1 means complete mismatch ($A_i \cap B_i = 0$, i.e. the polygons do not overlap) and 0 complete match ($A_i \cup B_i = A_i \cap B_i$, i.e. the polygons overlap perfectly).

The values of error registered in the first case study were used to rank the products. Under the assumption that a high informative content allows interpreters to map the landslide most closely

to the benchmark, this ranking orders the images from the lowest to the highest informative content. To limit possible learning effects (*Fiorucci et al., 2018*), in the second test case interpreters were asked to map the landslide starting from the image that ranked worst in the first test case.

Finally, it must be considered that the SRTM 1 Arc-Second Global DTM used for Terrain Correction (see §2.2) has a coarse resolution (~30 m), which implies that there may be locally some geo-location errors and/or geometric distortions related to orthorectification that may introduce errors, especially in high mountain areas. However, these errors are not supposed to influence the maps comparison, since the images are all coregistered and possible errors would be common to all the maps.

3   Case studies

The first case study is a rock slide - debris flow - mudflow occurred in Villa Santa Lucia, Los Lagos Region, Chile on 16 December 2017. In the 24 hours before the landslide occurrence, a 120 mm rainfall was recorded after a two-weeks period of anomalous high temperatures which induced a rapid snowmelt (*Duhart et al., 2019; Mondini et al., 2019*). The landslide covers an area of 5.06 km^2, is over 9 km long and its width is around 30 m in its narrowest point and 1,200 m in its widest. The Santa Lucia landslide (**Figure 4**) started as a rock slide, developed as a debris flow and ended as a mudflow that killed 11 people in the town downhill. The landslide estimated volume is 7.2 million cubic meters and its highest speed reached 20 m/s (*Duhart et al., 2019*). The landslide travelled downhill along a slope facing towards ESE, it climbed uphill on the opposite slope of the Burrito valley for about 1 km, and then flowed into the valley towards South, eventually forming a fan-shaped deposit that partially destroyed the Santa Lucia village.

According to *Duhart et al (2019)*, the source area of the Villa Santa Lucia landslide is characterised by a Pleistocene volcanic complex mainly composed of deeply altered volcanoclastic deposits, and exhibiting a subvertical fracturing. The volcanic sequence is sub-horizontal and overlaid on an intrusive mafic sequence. The outcrops show diffuse evidence of glacial activity. Structurally, this region is characterised by the presence of a regional fault zone (the Liquiñe-Ofqui Fault Zone) whose main superficial expression is the Villa Santa Lucia valley. The structural setting, the deep alteration and fracturing conditions of the geological layers in this area can be considered the main predisposing factors of the Villa Santa Lucia landslide. The high water content due to the rainfall and snowmelt event caused the evolution of the initial rock slide into a debris flow - mudflow.

This landslide has deeply changed the land cover, since a large part of the woods was transported downhill. As a result, a very clear morphological and radiometric "scar" was left. In the upper part of the landslide, that is along the slope facing ESE, the landslide shows not only a radiometric signature/scar but also a strong morphological fingerprint, which consists in a large missing volume in the upper part and a large deposit at the foot of the slope. Here, the hydrographic network appears destructured, with the main valley being featured by shallow ephemeral channels. The area where the landslide climbed uphill the opposite slope appears smoother and the main signature is mostly radiometric. In the area where the landslide entered the Burrito valley the images are featured by much shadow that hampers to make out the valley bottom. Finally, the fan area appears very obvious on optical images. It interrupts the colour and pattern of the vegetation, and the roads network, which was locally covered by a three-meter
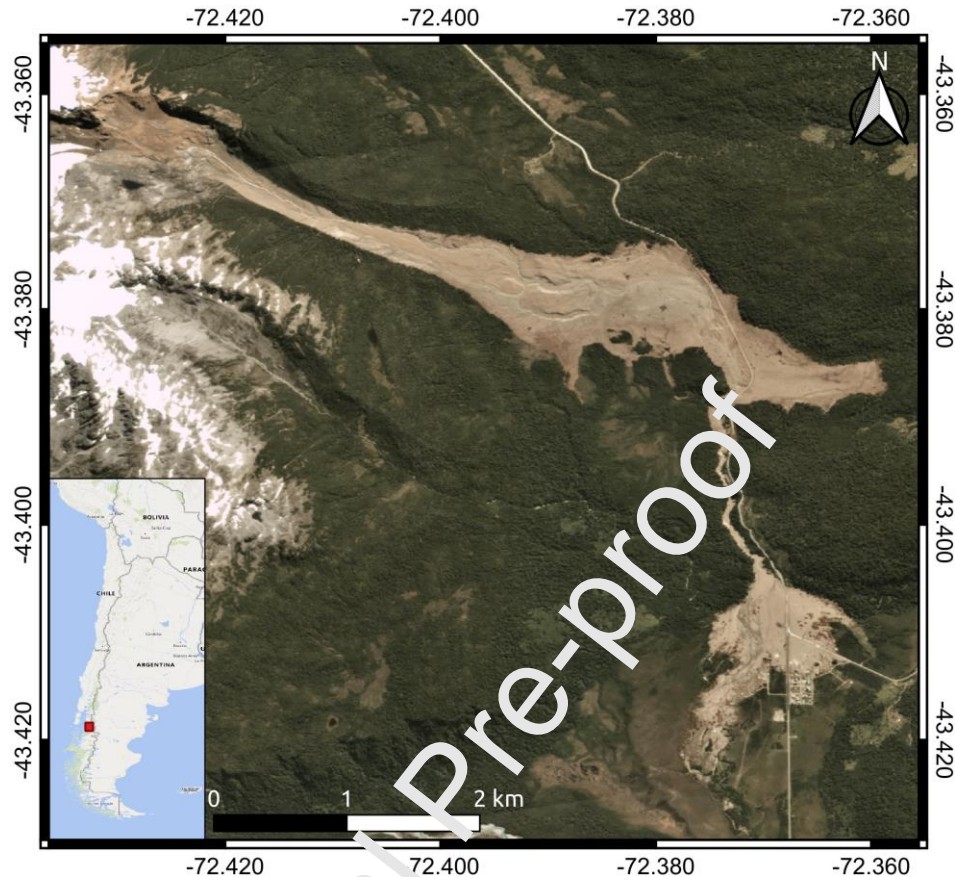
thick mud layer.

Figure 1 - Location map of the Santa Lucia landslide, Chile. Location map source: BingMaps™. Post-event image source: PlanetScope OrthoTile taken on 27 February 2018 (www.planet.com).

The second case study is a rock slide occurred in early August 2015 in the Tonzang region, Chin Division, Myanmar (**Figure 2**). The Government of the Republic of the Union of Myanmar reported that torrential rainfall of the monsoon period hit Myanmar since July 16, and they were followed by Cyclone Komen in early August, which caused strong winds and exceptionally heavy rains (*The World Bank, 2015; Mondini, 2017; Alvioli et al., 2018; Mondini et al., 2019*). It is reported that in the Chin Division the rainfall event was extreme, exceeding a 1,000 years return period event (*The World Bank, 2015*).

Such a triggering event caused thousands of landslides (*The World Bank, 2015; Alvioli et al., 2018; Mondini et al., 2019*), the largest of which appears to be the Tonzang landslide, which covers an area of 6.25 km^2, is over 6 km long and its width is around 1 km. The Tonzang landslide deeply changed the local morphology. Three new lakes developed along the slope where it occurred, one large lake developed along the main river which was dammed with an estimated 90 m thich deposit, and a new lake was also developed by deposit along the tributary that enters the main river from North. There is a long runout probably amplified by the contribution of other landslides triggered by the same rainfall event.

The Tonzang landslide developed within a Cretaceous Flysch sequence that includes limestone

layers (*Zaw et al; 2017*), on an orthoclinal/cataclinal-dip slope. The landslide may therefore have started as a translational slide that exploited the primary discontinuities of the stratigraphic sequence.

Like the Chile test case, this landslide deeply changed the local land cover, formerly forested. Differently from the Chile test case, the Tonzang landslide developed entirely along a slope facing towards NNE (**Figure 2**). In more detail, it moved towards North in its upper part, and towards NE in its lower part. These two sections divide the landslide roughly in two zones of comparable size. The landslide caused relevant morphological changes, with a large scarp, roughly corresponding to the upper half N-facing, and most of its large missing volume was deposited downhill. The head of the deposit shows three small lakes, whereas two lakes formed downhill, one along the main river, West of the deposit, and one North of the deposit, along a tributary of the main river. Similarly to the Chile event, the hydrographic network appears disrupted.

Figure 2 shows a post-event image acquired by the RapidEye at 6.5 m resolution (5 m corresponding to orthorectified images) acquired on 5 January 2016.
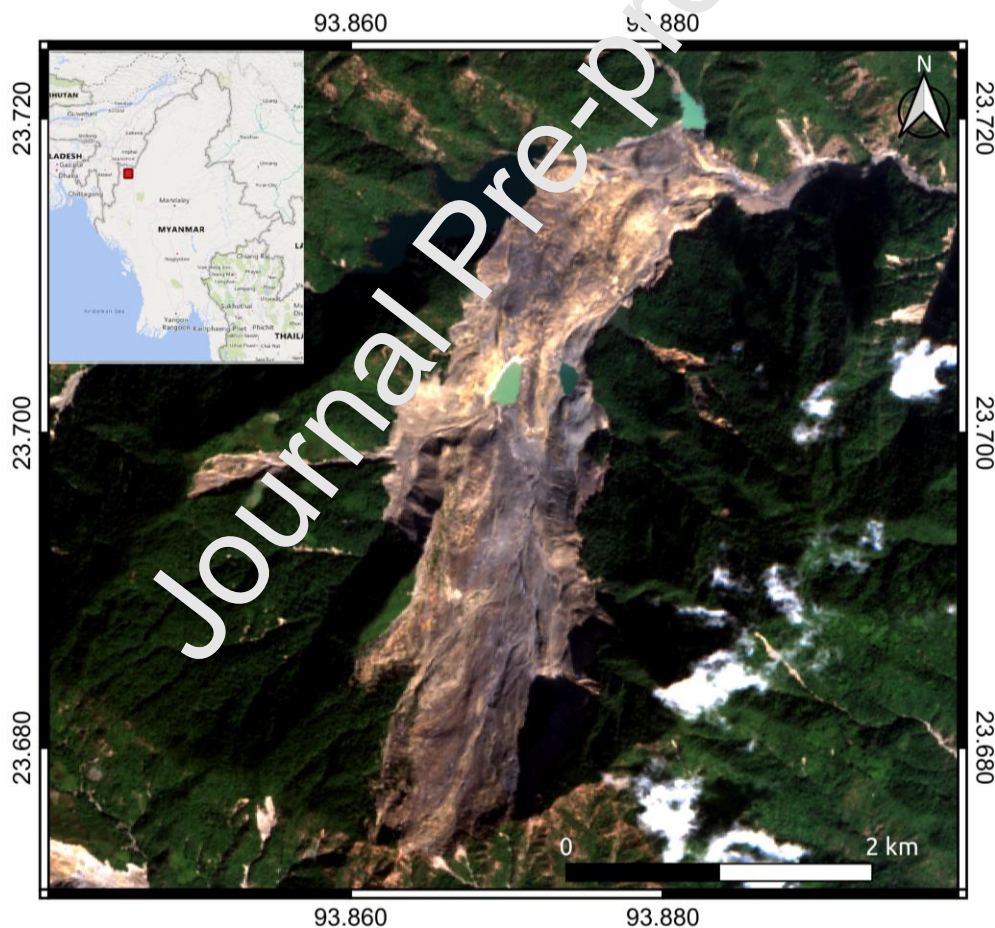

Figure 2 - Location map of the Tonzang landslide, Myanmar. Location map source: BingMaps™. Post-event image source: RapidEye satellite image with 6.5 m resolution (5 m corresponding to orthorectified images) acquired on 5 January 2016.

For the Chile test case (Villa Santa Lucia landslide), a total of 72 images were analysed (**Figure 1**): 24 images of β_0Log-Ratio were prepared, and 24 couples of pre-event and post-event images, whereas for Myanmar (Tonzang landslide) the ascending images in the VH polarisation were unavailable. This led to a total of 54 images (**Figure 2**): 18 images of change (β_0Log-Ratio), and 18 couples of pre-event and post-event images. **Table 1** reports the dates of acquisition of the original SAR images, the optical images, and the date of occurrence of the landslide event.

Table 1 - Dates of acquisition of the SAR images for the two sites. Event date is also reported.

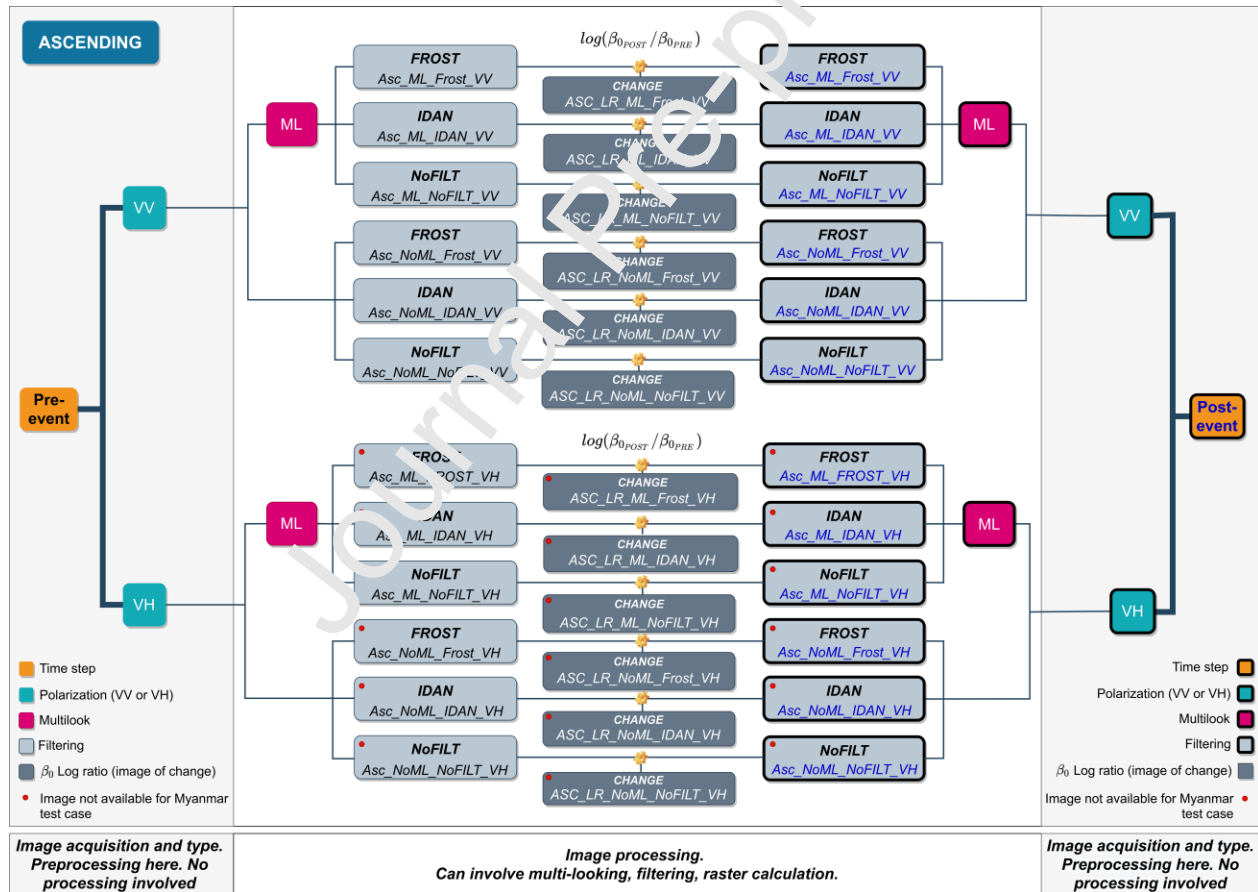|		SAR				Optical
		Pre-event		Post-event		Post-event
Landslide	Event date	Ascending	Descending	Ascending	Descending	
Villa Santa Lucia	16/12/2017	28/11/2017	12/12/2017	22/12/2017	24/12/2017	27/2/2018
Tonzang	Early August 2015	18/7/2015	2/6/2015	11/?/2015	17/11/2015	5/1/2016

Figure 3 - Scheme of the SAR images available for the two test cases for the Ascending acquisition geometry. Thick lines connect different image characteristics by acquisition. Thin lines connect images linked by pre-processing steps. Black outlined boxes refer to post-event acquisition, as opposed to non-outlined boxes. Red circles mark images not available for the Myanmar test case. Image names are reported
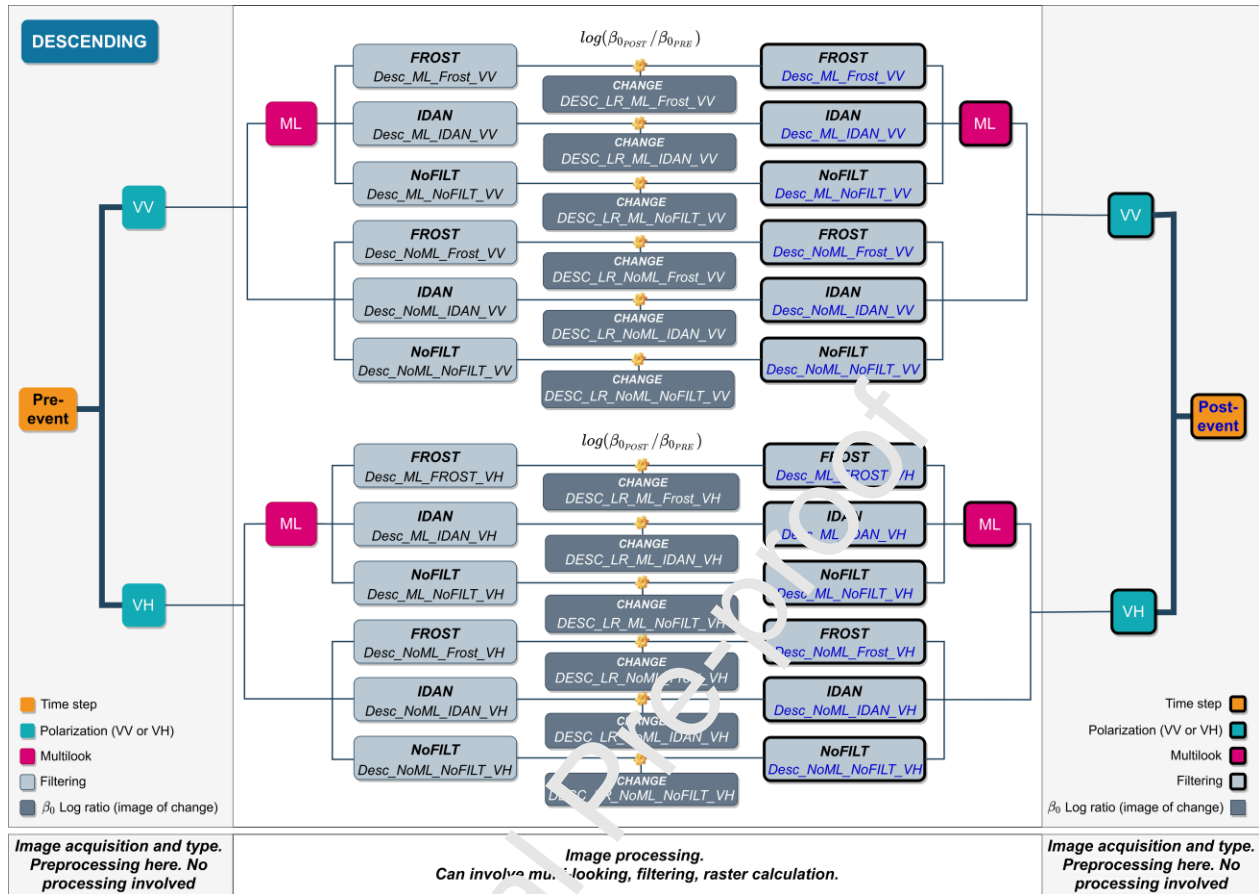
according to **Table A1**.

Figure 4 - Scheme of the SAR images available for the two test cases for the Descending acquisition geometry. Thick lines connect different image characteristics by acquisition. Thin lines connect images linked by pre-processing steps. Black outlined boxes refer to post-event acquisition, as opposed to non-outlined boxes. Image names are reported according to **Table A1**.

Figure 5 and **Figure 6** show how the Villa Santa Lucia landslide appears in Ascending (**Figure 5**) and Descending (**Figure 6**) acquisition geometries, according to the multilook pre-processing application and the filtering technique. Images are all visualised stretching the histogram between the 3rd and 93rd percentile of the pixel values distribution, which was also used for the interpretation.
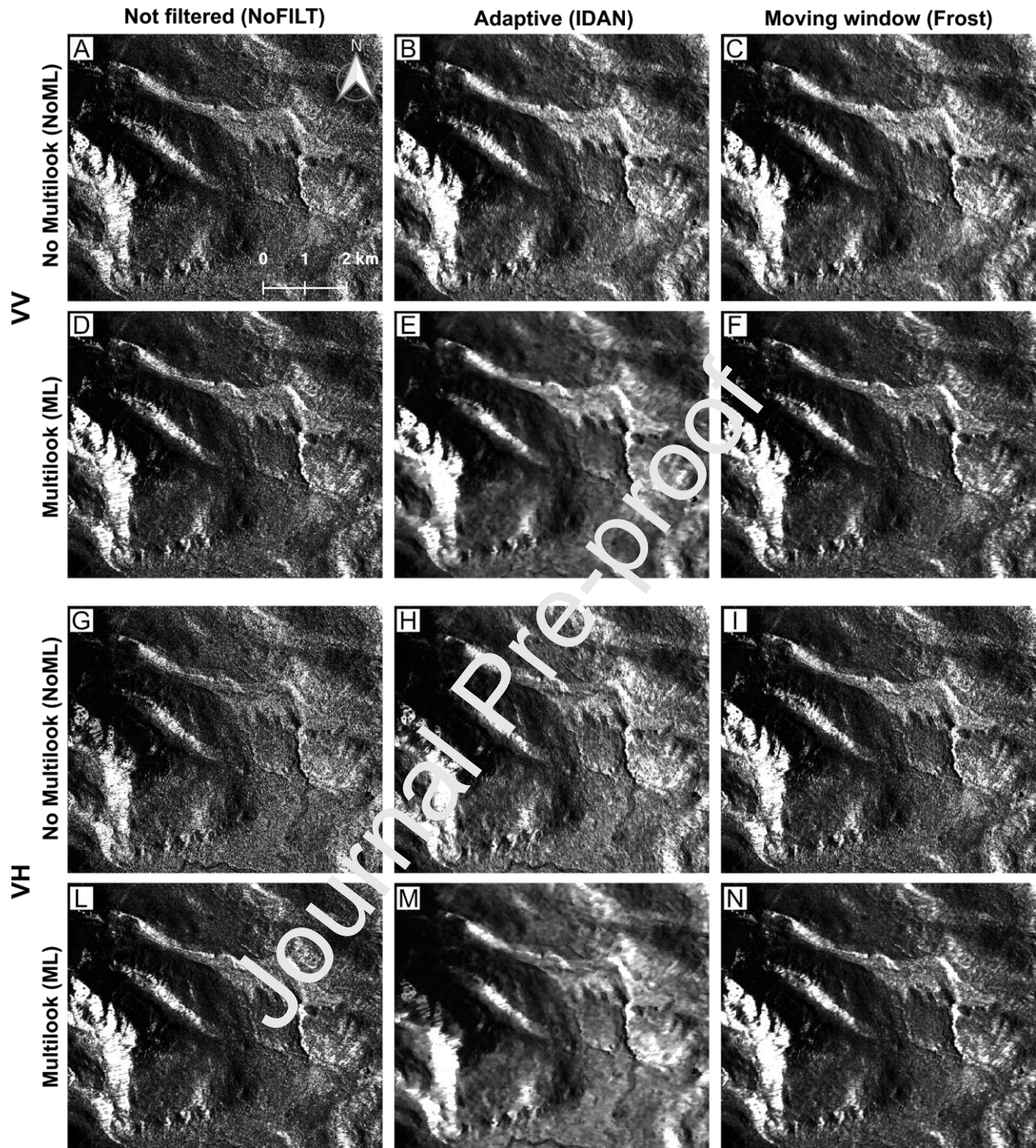
Figure 5 - Post-event images (Ascending) of the Villa Santa Lucia landslide (Chile). A to F, images in VV polarisation. G to N images in VH polarisation. In the matrix, images are represented based on the filter used (none, IDAN and Frost) and the multilook pre-processing application.
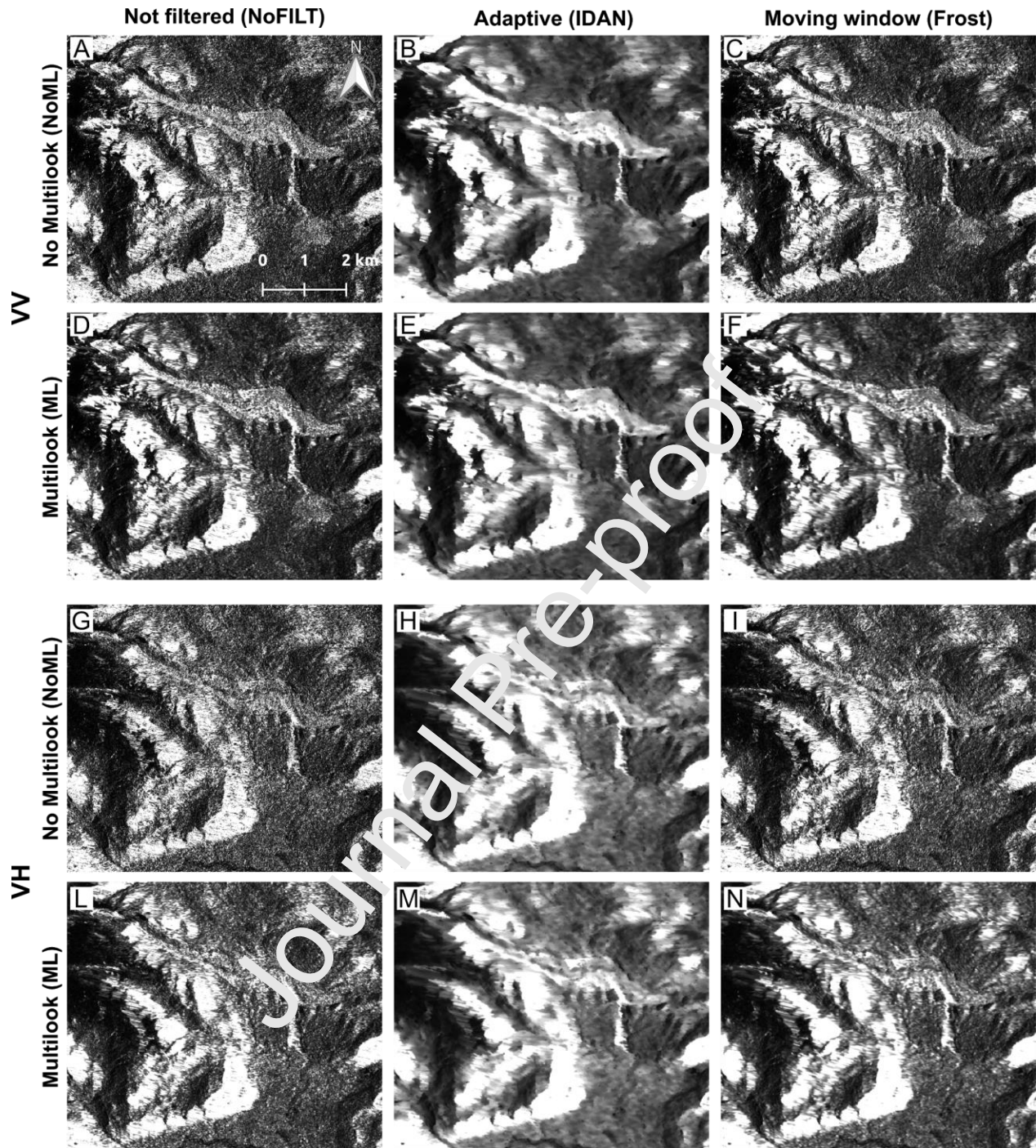
Figure 6 - Post-event images (Descending) of the Villa Santa Lucia landslide (Chile). A to F, images in VV polarisation. G to N images in VH polarisation. In the matrix, images are represented based on the filter used (none, IDAN and Frost) and the multilook pre-processing application.

Figure 7 and **Figure 8** show the Villa Santa Lucia landslide in the images of change of the backscatter coefficient. The same histogram stretching has been applied as for the post-event images.
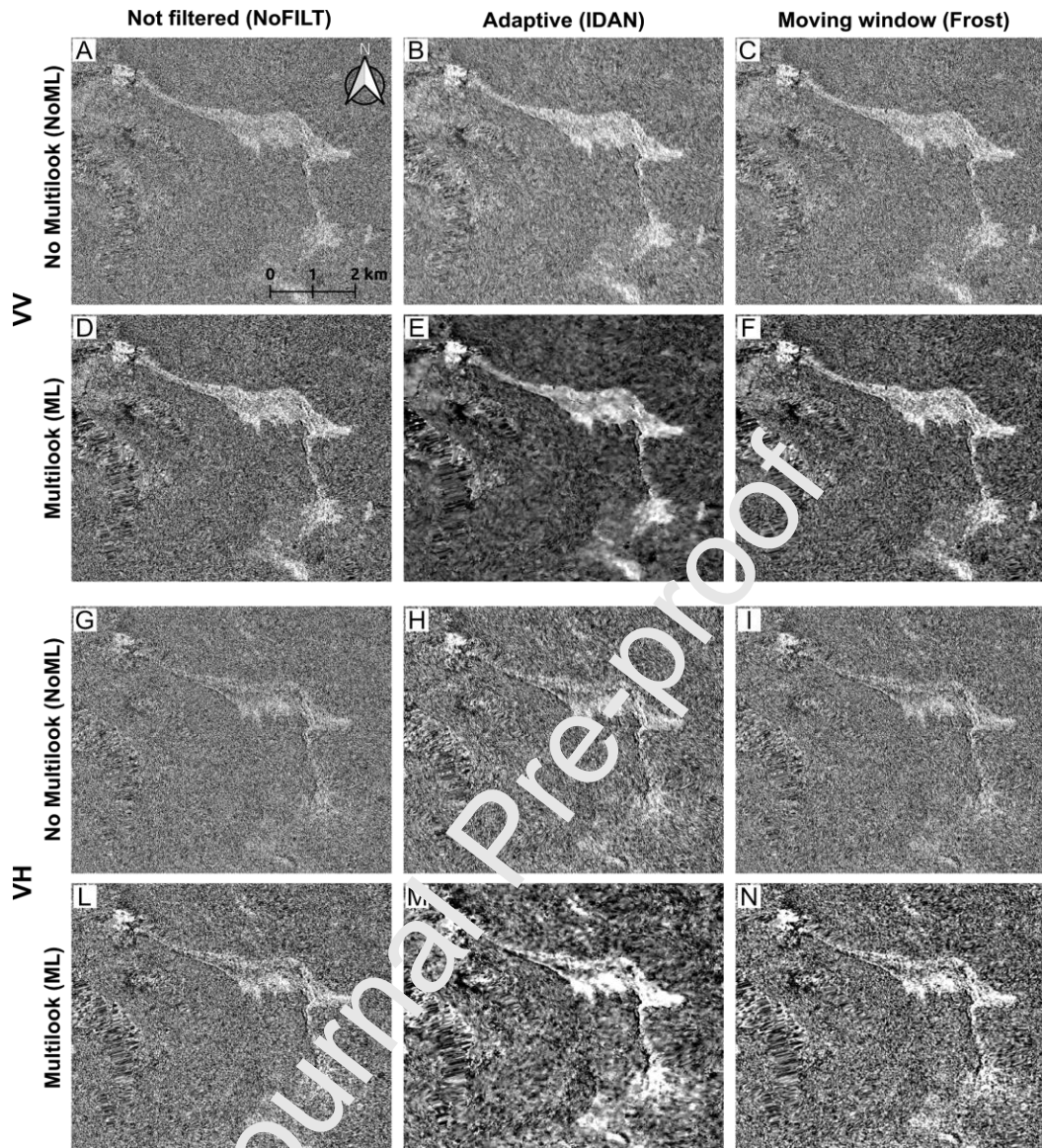
Figure 7 - Images of change (β_0 Log-Ratio), Ascending, of the Villa Santa Lucia landslide (Chile). A to F, images in VV polarisation. G to N images in VH polarisation. In the matrix, images are represented based on the filter used (none, IDAN and Frost) and the multilook pre-processing application.

Figure 8 - Images of change (β_0 Log-Ratio), Descending, of the Villa Santa Lucia landslide (Chile). A to F, images in VV polarisation. G to N images in VH polarisation. In the matrix, images are represented based on the filter used (none, IDAN and Frost) and the multilook pre-processing application.
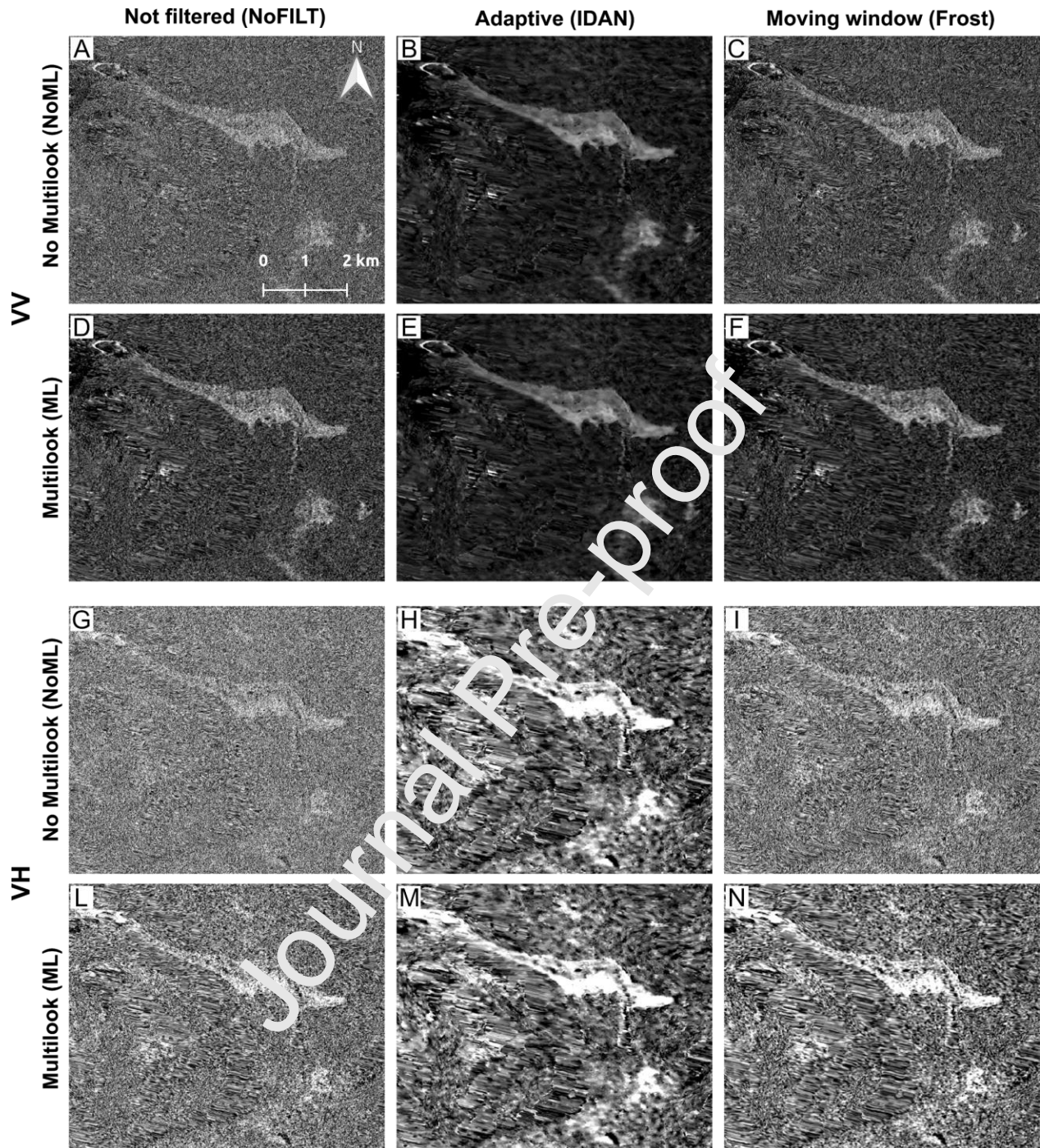
Figures 9 to 11 show how the Tonzang landslide appears in SAR images used for the second test case, namely (i) in the Ascending geometry (only VV polarisation was available, **Figure 3**), both post-event (**Figure 9A-F**) and change of the backscatter coefficient (**Figure 9G-N**), and (ii) in the Descending geometry, both post-event (**Figure 10**) and change of the backscatter coefficient

(**Figure 11**). In the images, the same histogram stretching was applied as for the Santa Lucia landslide (i.e., the Chile test case): histogram stretching between the 3rd and 93th percentile of the pixel values distribution, which was also used as base value for the interpretation.
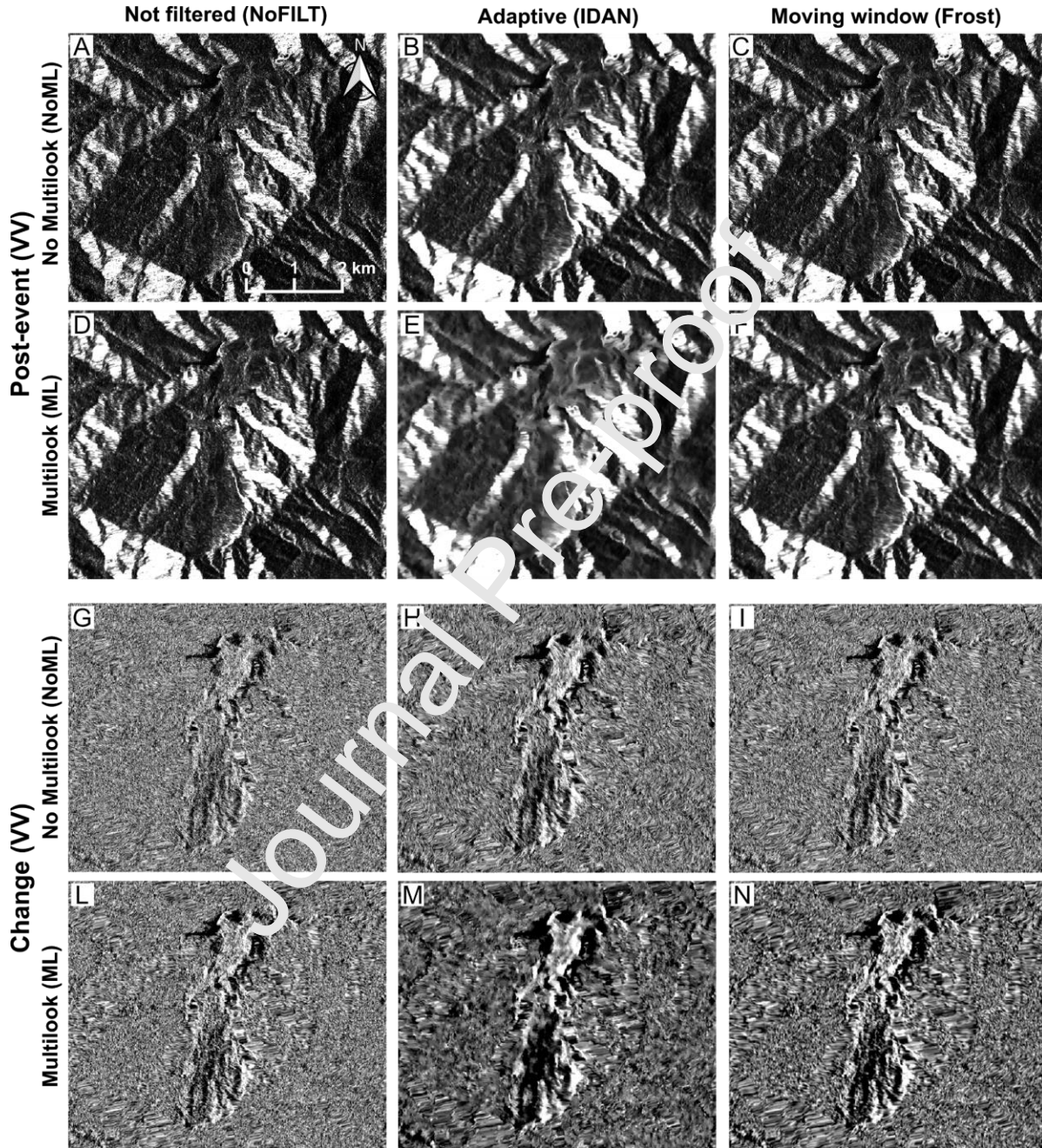

Figure 9 - A to F, post-event images (Ascending) of the Tonzang landslide (Myanmar) in VV polarisation. G to N, images of change (β_0 Log-Ratio) of the same landslide. In the matrix, images are represented based on the filter used (none, IDAN and Frost) and the multilook pre-processing application. Images in VH polarisation were not available (**Figure 3**).
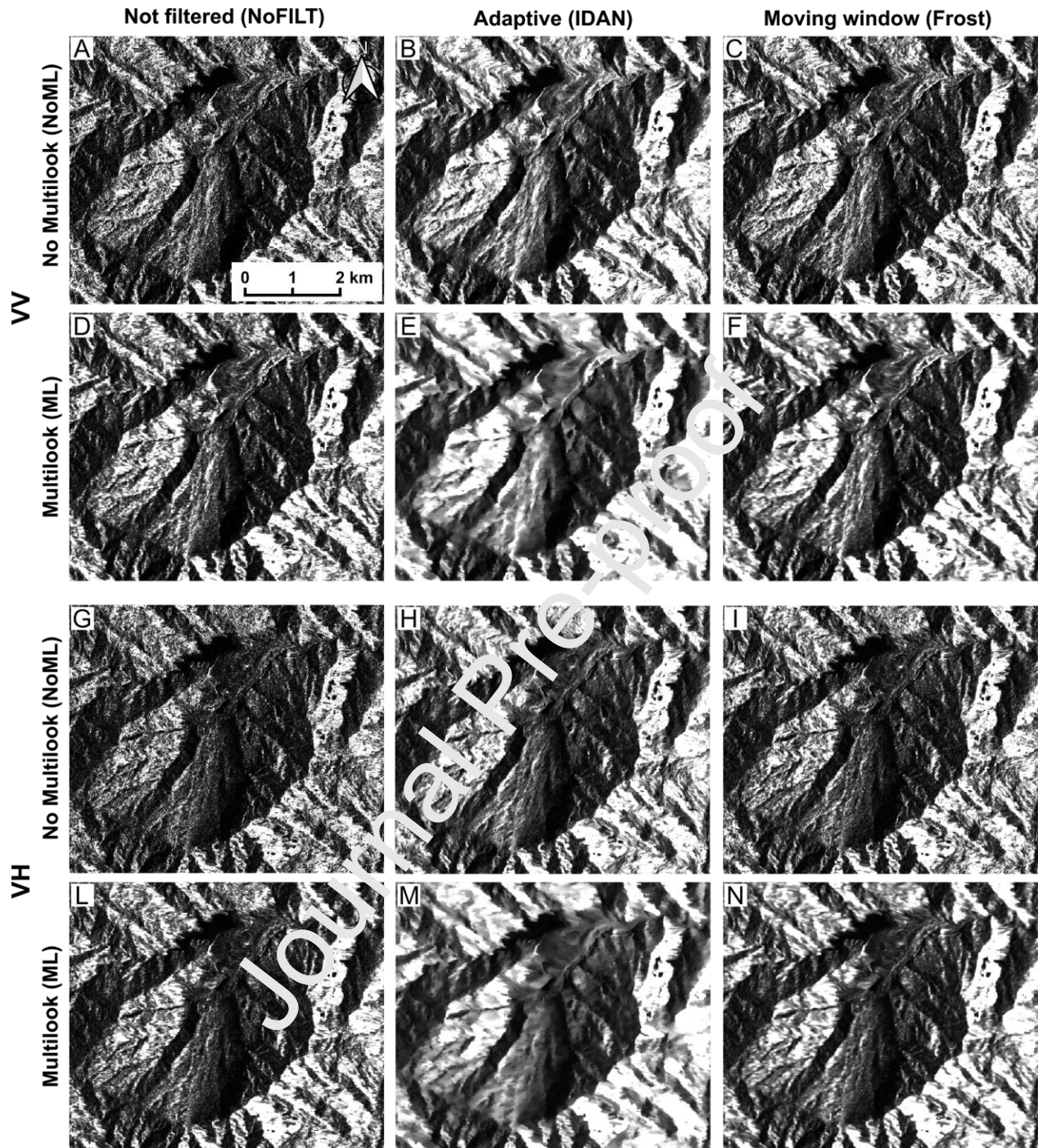
Figure 10 - Post-event images (Descending) of the Tonzang landslide (Myanmar). A to F, images in VV polarisation. G to N, images in VH polarisation. In the matrix, images are represented based on the filter used (none, IDAN and Frost) and the multilook pre-processing application.

Figure 11 - Images of change (β_0 Log-Ratio), Descending, of the tonzang landslide (Myanmar). A to F, images in VV polarisation. G to N images in VH polarisation. In the matrix, images are represented based on the filter used (none, IDAN and Frost) and the multilook pre-processing application.
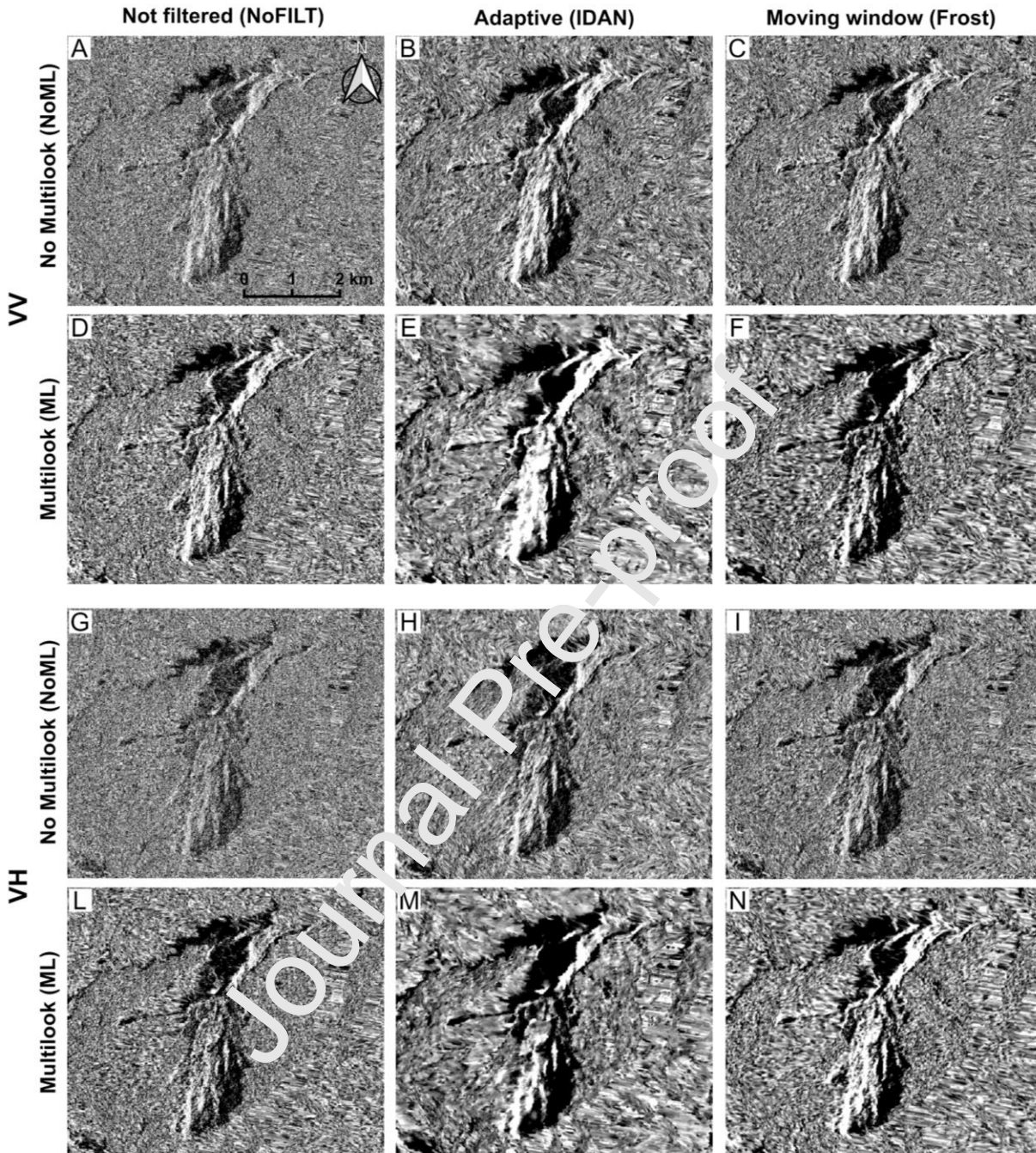
4   Results

The Santa Lucia landslide was mapped by the team of interpreters using the 72 images available

(**Figure 3**, **4**). In particular, a total of 48 maps were obtained: 24 through the interpretation of post-event images (**Figure 5, 6**) and 24 through the interpretation of the LR images (**Figure 7,8**). **Figure 12** shows the ensemble of the 48 polygons drawn by the interpreters, compared to the benchmark (red outlined polygon), obtained through an a priori interpretation of the optical post-event image.

Area of landslide polygons mapped in SAR images ranges between 3.58 km^2 and 5.41 km^2 (σ=0.44 km^2, μ=4.62 km^2), with a median of 4.63 km^2. Area of the benchmark is 5.06 km^2. **Figure 12** shows the geographical distribution of landslide polygons mapped in SAR images and the benchmark derived from the optical image. Inspection of **Figure 12** reveals that the dispersion of the SAR derived maps is not homogeneous, but mostly concentrated in the scarp area and in the fan area. Inset of **Figure 12** shows the degree of geographic dispersion of landslide polygons. The inset map is the result of a kernel density estimation run on points extracted every 50 meters along the landslide polygons. The kernel density was run using *v.kernel* tool in GRASS GIS (*GRASS Development Team, 2017*) and shows the number of points within a search radius of 100 meters. The density map is used as a proxy of the consistency of the maps obtained in SAR images. The higher the density, the closer the landslide borders are to each other. The lower the density, the higher the dispersion of the maps. The map has been used to separate three domains of the landslides (scarp, body, and fan, separated by dashed black lines in **Figure 12**), based on a combined criterion that takes into account the overall density and landslide morphology.
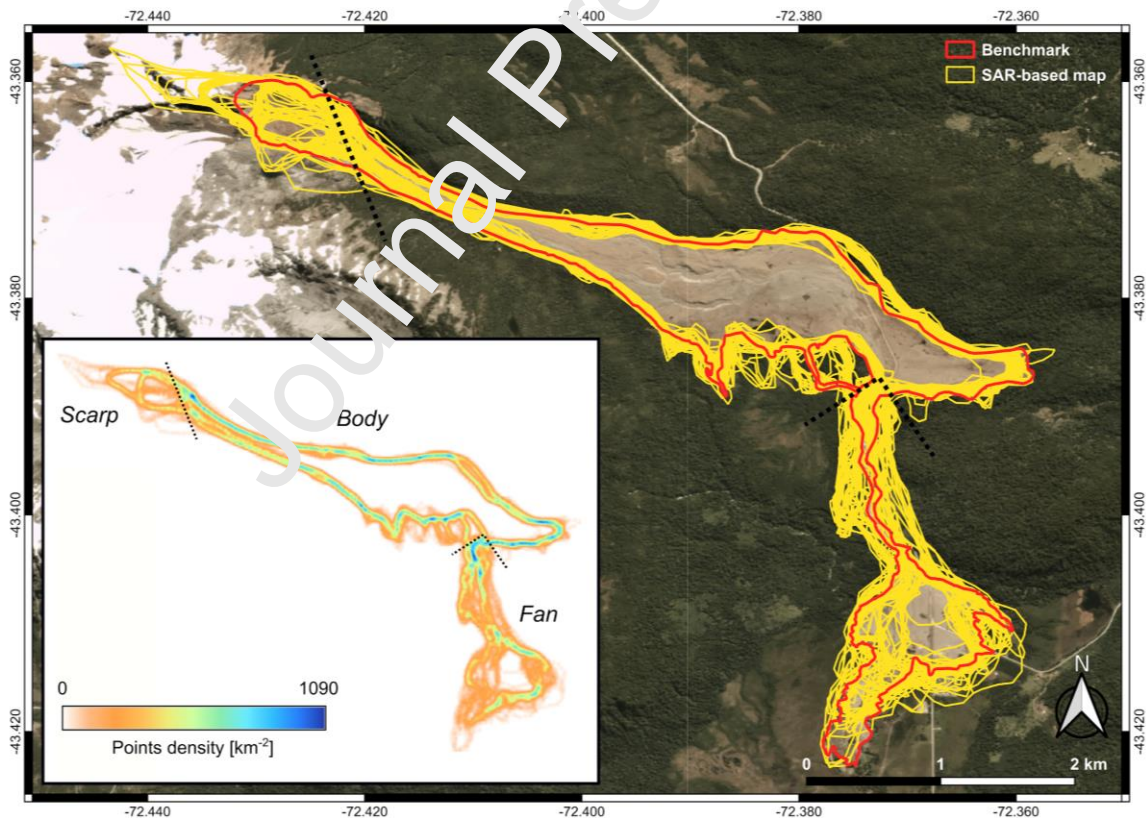

Figure 12 - Main image: comparison of the maps of the Villa Santa Lucia landslide (Chile) obtained through interpretation of SAR images (yellow outlined polygons) and the benchmark, i.e., the map obtained through interpretation of the optical post-event

image (red outlined polygon). For reference, the optical post-event image is shown in **Figure 1**. Inset: kernel density map obtained by running a kernel density over points sampled each 50 m along the boundary of landslide polygons mapped in SAR images.
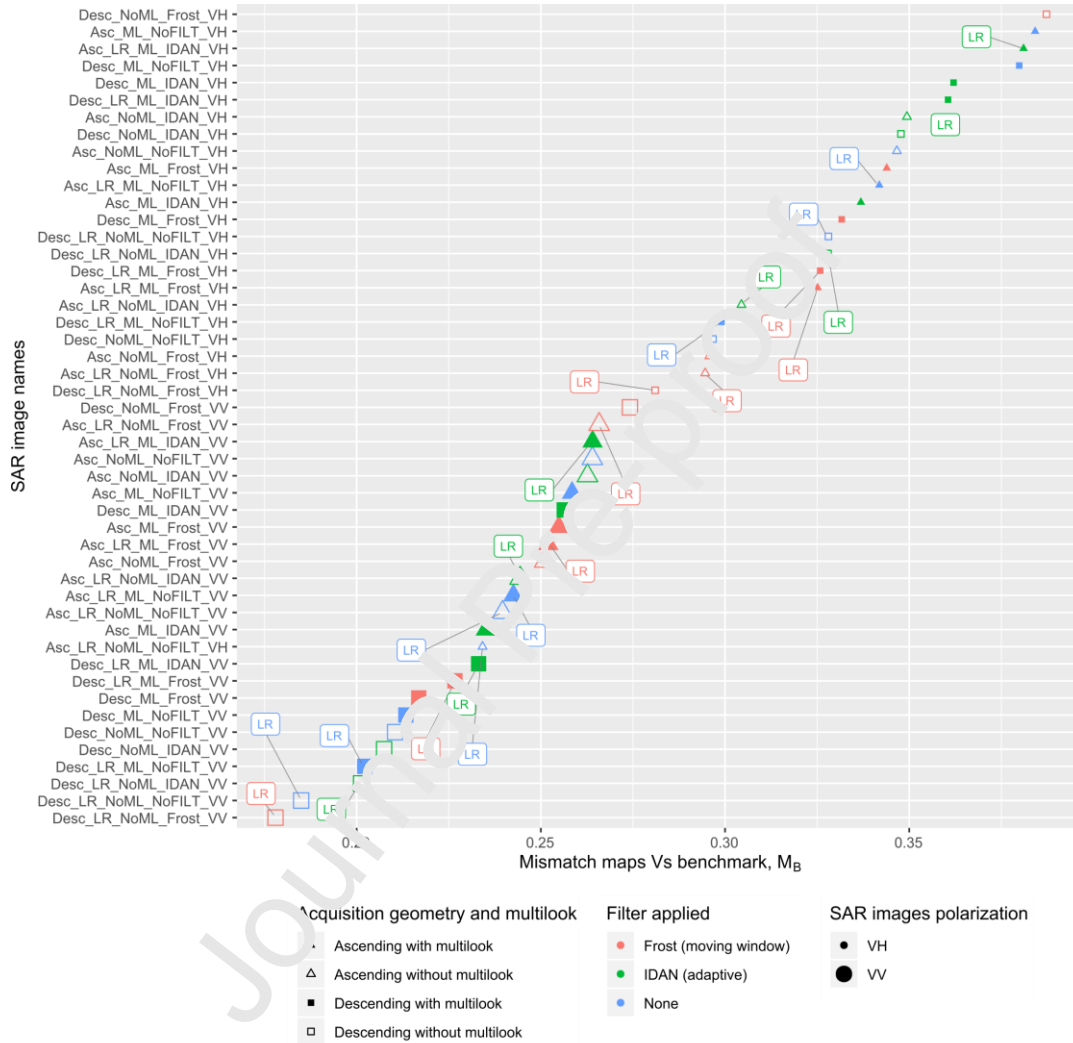

Figure 13 - Distribution of the mismatch between the SAR derived maps of the Villa Santa Lucia landslide compared to the benchmark. Data points are ranked by mismatch value (X axis), whereas the corresponding SAR images names are reported on the Y axis, according to the names listed in **Figure 3**, **Figure 4** and **Table A1**.

Plot in **Figure 13** shows the distribution of the values of the mismatch between SAR maps and the benchmark (M_B), and **Table 2** summarises the main parameters of its statistical distribution. In the plot, each data point is represented based on the SAR image characteristics: multilook application (not applied, empty symbols; applied, filled symbols), filter type (Frost, red symbols; IDAN, green symbols; None, blue symbol), polarisation (VV, large symbols; VH, small symbols), geometry of acquisition (ascending, triangles; descending, squares), and whether interpreters used LR images (label "LR") or post-event images. Inspection of **Figure 13** reveals a

sharp subdivision (around the 50th percentile) of the mismatch values based on the polarisation, with VV images that correspond to the lowest 50% of the M_B values distribution. In sub-order, descending images (squares) correspond to lower values of mismatch compared to ascending ones (triangles). For example, over 40% of the VV images data points correspond to maps prepared from descending images. In further sub-order, images of change and images without multilook seem to correspond to maps with relatively lower mismatch as opposed to post-event images and images with multilook applied.

Table 2 - Descriptive statistics of the landslide maps prepared for the two test cases. Data are also shown separately for the three sectors of the Villa Santa Lucia landslide.

Landslide	Mismatch, M_B				
	Min	*Max*	*Mean*	*Median*	*Sd*
Villa Santa Lucia	0.178	0.387	0.284	0.274	0.058
Villa Santa Lucia (scarp)	0.245	1.000	0.471	0.369	0.218
Villa Santa Lucia (body)	0.099	0.258	0.172	0.172	0.039
Villa Santa Lucia (fan)	0.309	0.842	0.494	0.473	0.123
Tonzang	0.113	0.294	0.178	0.168	0.050

Figure 14 shows six examples of the maps and their location within the distribution of M_B in the empirical cumulative distribution function (ECDF). It is evident that different geographical mismatches correspond to similar mismatch values. Inspection of the images reveal that the most of the mismatch is concentrated in the scarp area and in the fan, whereas the central portion of the landslide was delineated almost always close to the benchmark. This evidence is also confirmed by inspection of **Figure 13**.
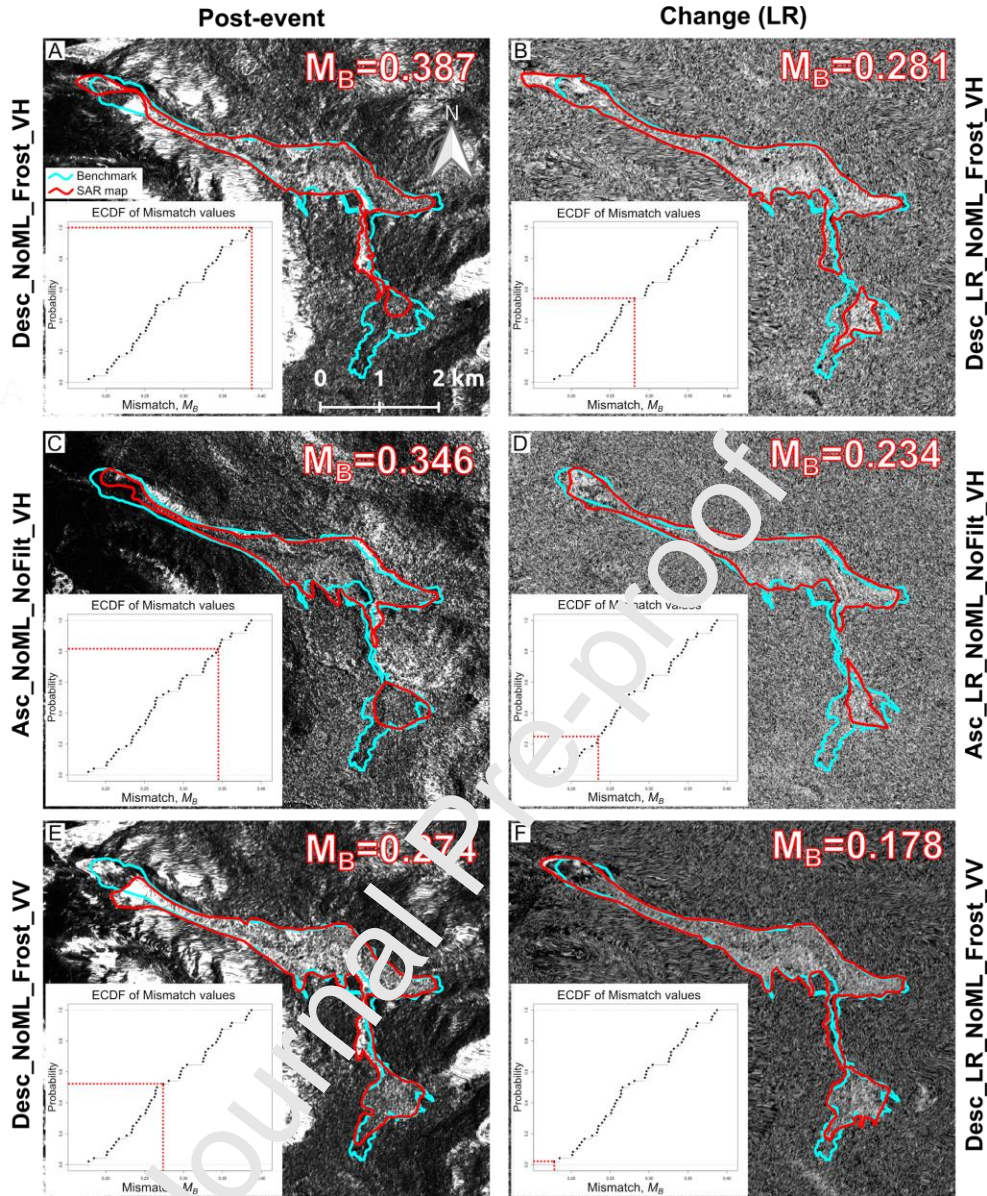
Figure 14 - Comparison of six maps of the Villa Santa Lucia landslide. In each image it is shown: the benchmark (cyan outlined polygon), the SAR map (red outlined polygon), the mismatch value M_B (top right), the location of the M_B value within the plot of the Empirical Cumulative Distribution Function (ECDF) of the mismatch values (bottom left). Left column: post-event images. Right column: corresponding images of change. Rows title: name of the image (as in **Figure 3**, **Figure 4** and **Table A1**).

The Tonzang landslide was mapped using the 54 images available (**Figure 3** and **Figure 4**). In particular, a total of 36 maps were obtained: 18 through the interpretation of post-event images (**Figure 9A-F,10**) and 18 through the interpretation of the LR images (**Figure 9G-N,11**). **Figure 15** shows the ensemble of the 36 polygons drawn by the interpreters, compared to the benchmark (red outlined polygon), obtained through interpretation a posteriori of the optical post-event image.
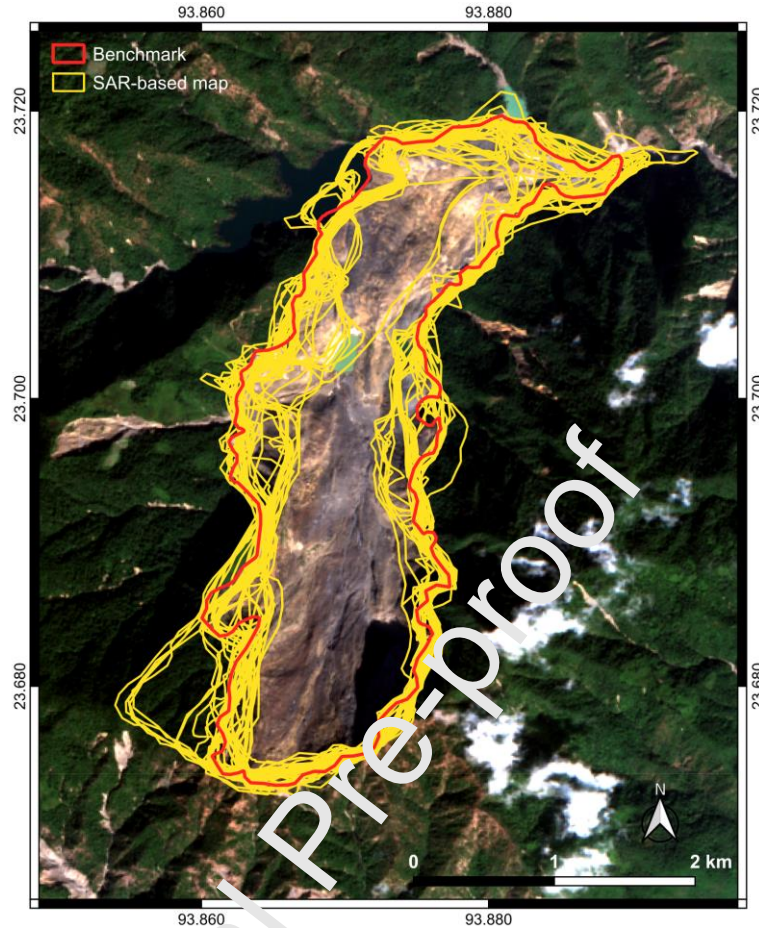
Figure 15 - Comparison of the maps of the Tonzang landslide (Myanmar) obtained through interpretation of SAR images (yellow outlined polygons) and the benchmark, i.e., the map obtained through interpretation of the optical post-event image (red outlined polygon). For reference, the optical post-event image is shown in **Figure 2**.

Area of landslide polygons mapped in SAR images ranges between 3.82 km^2 and 5.41 km^2 (σ=0.4 km^2, μ=4.73 km^2), with a median of 4.77 km^2. Area of the benchmark is 6.25 km^2. Inspection of **Figure 15** reveals that the dispersion of the SAR derived maps is higher in the central part of the landslide and at the toe. A few polygons show a large mismatch in the scarp area, where a portion of the slope which was not involved in the landslide was included in the maps.

Figure 16 shows the distribution of M_B for the Tonzang landslide, main values of the statistical distribution of M_B are reported in **Table 1**. Inspection of **Figure 16** reveals that the images in the first quartile of the distribution are all descending (squares) and that the 64% (i.e., 9 out of 14) are images of change and/or images in VV polarisation. As for the Chile test case, a quite sharp subdivision of the M_B distribution can be observed, but, in this case the most discriminant characteristic is the acquisition geometry, whereas polarisation plays a secondary role. In particular, only one value out of the first 50th percentile of M_B distribution corresponds to a map produced from an ascending image. Furthermore, images of change correspond mostly to low

mismatch values, since 66.7% of maps produced from LR images have M_B smaller than 0.2. Polarisation seems to play a minor role in the clustering of values of M_B. Interestingly, the two images with the lowest mismatch are VH, which contrasts with the evidence of the Chile test case.
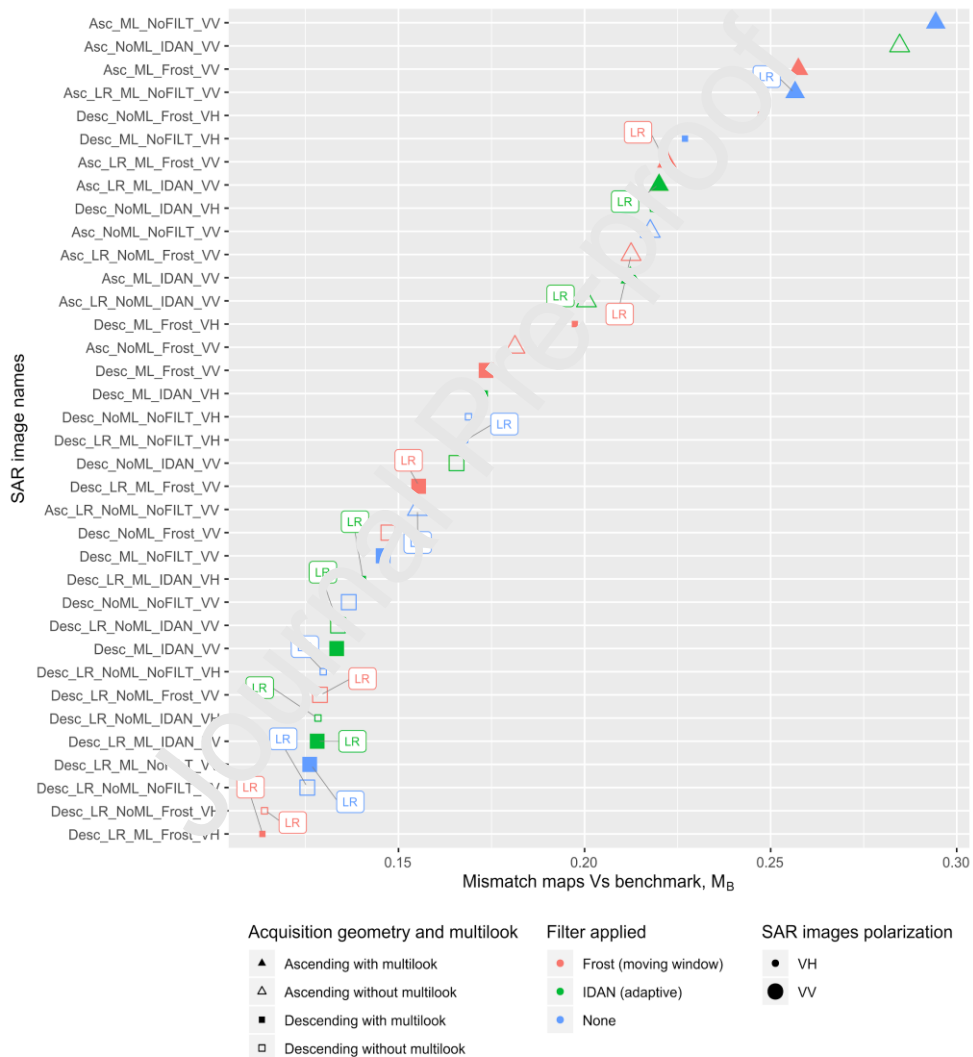

Figure 16 - Distribution of the mismatch between the SAR derived maps of the Tonzang landslide compared to the benchmark. Data points are ranked by mismatch value (X axis), whereas the corresponding SAR images names are reported on the Y axis, according to the names listed in **Figure 3**, **Figure 4** and **Table A1**.

Three main remarks have to be done. First, the experiment was led on two test cases, which were chosen because (i) they were detected in previous studies using SAR, and ranked as good test cases for testing landslide mapping (*Mondini et al., 2019*), (ii) they occurred in the observation time span of Sentinel-1 images, (iii) the Chile test case was an ideal training case to test images and interpreters capability in a range of different slope aspects, different landslide signatures, different land covers (iv) the Tonzang landslide is a large landslide that can be considered a simpler case compared to the Villa Santa Lucia landslide, and hence more appropriate for testing images and interpreters in preparing landslide maps simulating a landslide event scenario (v) they are large enough to guarantee that the resolution of the images is not an issue.

Second, the mismatch resulting from the comparison of each map with the benchmark has a component related to the relative positioning of SAR and optical images and a component related to the interpretation and mapping process, including unavoidable errors due to shadowing or layover. Since the SAR stacks are perfectly co-registered, the first component can be neglected because it is irrelevant to rank the relative mismatch (M_B) between the landslide maps.

Third, despite some possible accidental and systematic interpretation errors (that will be discussed in detail), we show that no severe biases by inconsistencies in the interpretation or by learning affect the results. The experiment was carried out by a team of four expert photo-interpreters (FB, FF, MC, MS). The formalisation of interpretation criteria as well as the mapping were carried out as a group and not individually, since previous research indicates "discussion" approaches as a tool to reduce subjectivity in the interpretation (*Guzzetti et al., 2012; Santangelo et al., 2014*). Despite the advantages of such approach, it has to be stated that some inconsistencies have occurred due to limited acquaintance with SAR amplitude derived products and limited access to ancillary data that could have reduced the ambiguities in case of doubts in the interpretation. Our data show that the highest mismatch for the entire map of the two landslides (**Table 2**) is equal to 0.387, a value which is lower than the mismatch usually obtained by maps produced by different interpreters (*Ardizzone et al., 2002*) and comparable to the mismatch characterising maps produced by the same interpreter using different techniques (*Santangelo et al., 2010, 2015*) or images (*Fiorucci et al., 2018*). This proves that bias by systematic inconsistencies in the application of interpretation criteria is limited in this experiment. Single cases will be discussed in detail. Furthermore, mismatch data (M_B) were plot according to the images viewing chronological order (**Figure 17**, **Table A1**) to understand if any bias by learning effect is present in our results. Inspection of **Figure 17A** reveals that interpreters were not influenced by their a priori knowledge of the landslide, as demonstrated by the sharp separation of data points by polarisation (i.e. by symbol size). Had the interpreters used their a priori knowledge to map the landslide, this trend would not have occurred, since interpreters read VV and VH images in an alternating sequence. Furthermore, **Figure 17B** shows that in the Myanmar test case (i) negative trends occur within data points grouped again by polarisation, (ii) a sudden increase in M_B marks the transition from VH to VV images, which again proves that learning effect is very limited, (iii) despite their order, descending images are systematically better performing than ascending ones. Since interpreters had no a priori knowledge in this case, we maintain that an increasing performance (i.e., lower M_B values towards right in the plot of **Figure 17B**) indicate more an increasing amount of information about this landslide than a learning process, which would be more a constant performance.
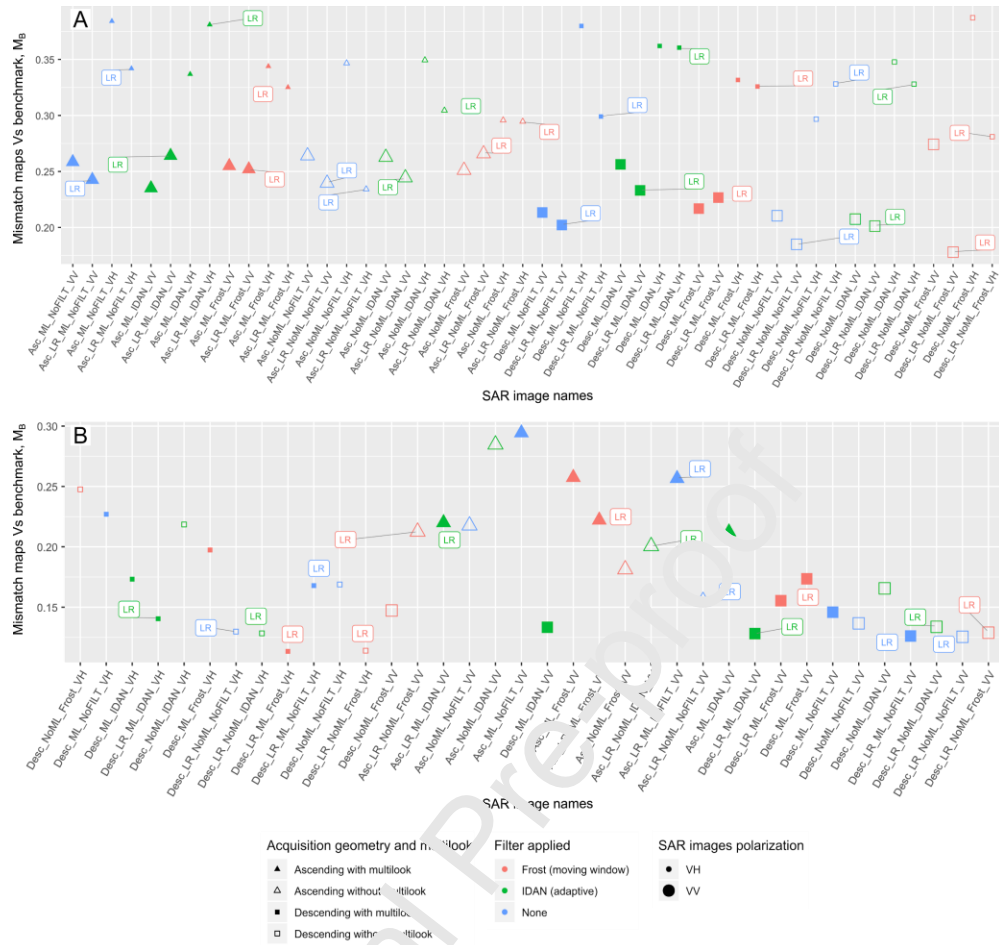
Figure 17 - Distribution of M_B (A) for the Villa Santa Lucia landslide and (B) for the Tonzang landslide. Data points are ordered by images viewing chronological order (X axis).

5 Discussion

5.1 Landslide detection and mapping in SAR backscatter products

In SAR images, the values of amplitude, and of the derived products, depend on the physical parameters of the backscattering land surface, including roughness, dielectric constant (i.e. soil moisture), and parameters related to the acquisition systems. In a single image, spatial changes in the amplitude can indicate different land covers, or local differences of the land cover physical properties, while temporal changes can be due to a sudden modification of the land cover, and these changes can be caused by the presence (in the first case), or the occurrence of a landslide (in the second case). These changes are seen by the interpreter as a variation of tones in the product and they can be used in the photo interpretative process, mirroring what is usually done when optical panchromatic or single channel images are used to detect/map landslides. A few pre-processing steps are meant to highlight, or smooth these changes of tones.

In the interpretation of the signal, also the PLIA variations should be taken into account. Other

conditions being equal, returns are normally stronger at low PLIAs and decrease with increasing incidence angles and then local changes in the backscattering properties in mountainous areas can be experienced according to the local morphology. The PLIA can be estimated using DEMs, and in general it is suitable to represent the pre-event conditions. Landslides can introduce variations difficult to extract from the image.

Figure 18 shows the landslide borders overlaid to the PLIA for the Chile test case. Inspection of the figure reveals that, locally, some errors appear to be common to groups of images, and cluster by acquisition geometry. For example, in the fan area, in descending images (white arrow in **Figure 18D**) the feeding channel is affected by a systematic error. Interpreters have consistently misinterpreted an element of the image that appeared white both in the post-event images and in the images of change (e.g., **Figure 14A,E**). That area corresponds to a nearly flat surface, possibly a river terrace on the hydrographic right of the valley. **Figure 18C,D** shows that the PLIA is very low in that location (15° - 20°) compared to the surrounding area (35° - 50°). Comparison of pre- and post-event images shows that pixel values have generally increased, which explains why this area was highlighted also in LR images (e.g., **Figure 14B,F**). To avoid this type of error, it is suggested that mapping be carried out by systematically checking not only changes in pixel values, but also pattern changes. By doing so, interpreters can avoid to include areas where the structure of the surface has not changed.

A systematic error is also found in the escarpment area, where the landslide scarp was mapped further upstream than its actual location (black arrow in **Figure 18D**). This happened only on descending LR VH images, where interpreters included an element which is morphologically compatible with the escarpment of a large landslide, given its position and curvature (e.g., **Figure 14B,E**). This is a case of morphological convergence (*Bucci et al., 2013; Gutiérrez and Soldati, 2018*), an ambiguity that is also common when mapping on stereoscopic optical images. We interpret this mapping error as the result of morphology, which causes the PLIA to be very low, and polarisation, since VH images are often characterised by a coarser grain of the images, which appears to the interpreters as a lower resolution image. To avoid this type of error, it is necessary to use other ancillary data that can reduce ambiguity. We suggest that images of different polarisation and acquisition geometry be compared when mapping event landslides on SAR amplitude derived products. However, it must be said that there is not always enough information to map landslides without uncertainty (*Santangelo et al., 2015*).
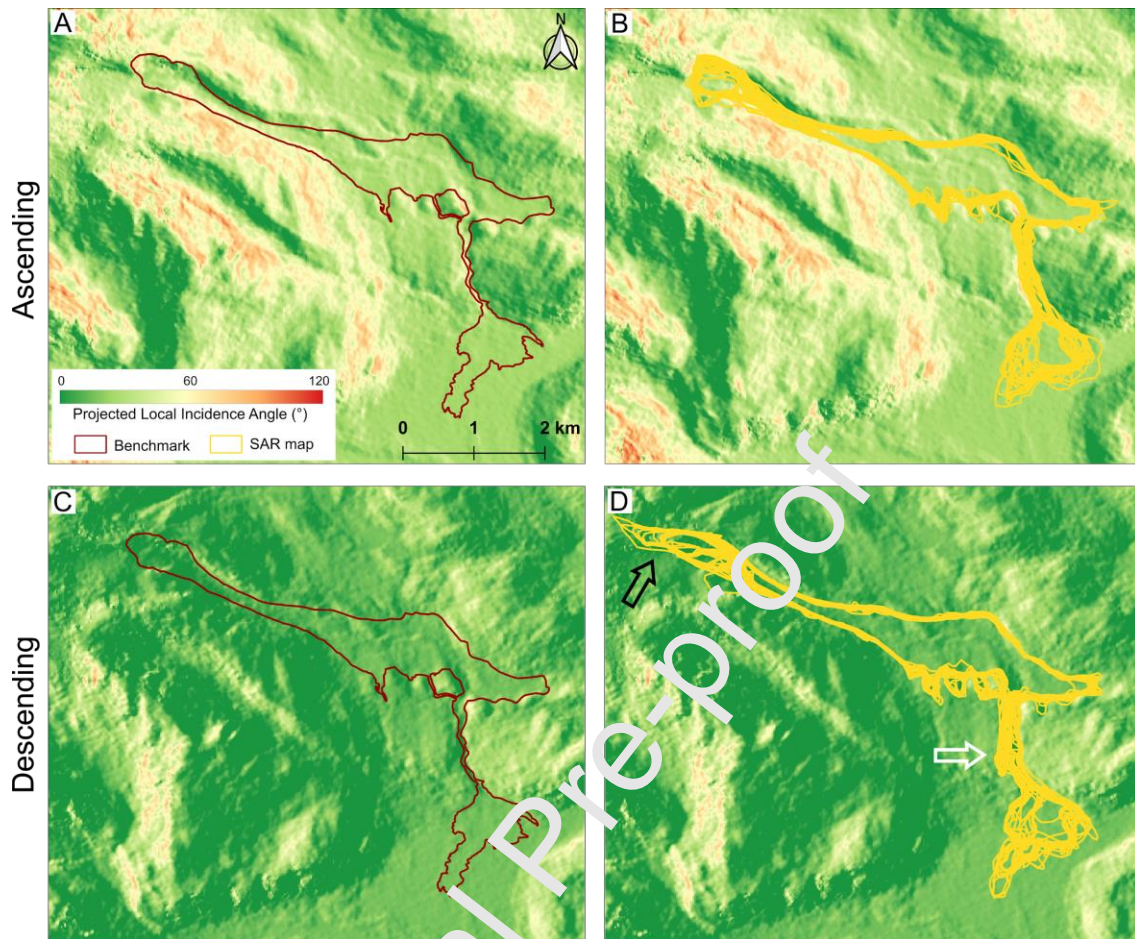
Figure 18 - Maps of the Projected Local Incidence Angle (PLIA) of the Chile test case, Ascending (A, B) and Descending (C and D). Benchmark and SAR maps are shown for reference. Figure B shows only maps prepared using ascending images; D shows only maps prepared on descending images. White arrow indicates a systematic error in the area of the feeding channel of the fan. Black arrow indicates a systematic error in the scarp area.

Comparing the PLIA in the ascending and descending images of the Chile test case, it appears also that the landslide borders are more clustered in descending images, where the PLIA is lower almost everywhere compared to ascending images. Our interpretation of this evidence is that the stronger returns of the SAR amplitude signal translate in a sharper contrast where change has occurred compared to undisturbed areas, which helps interpreters to be consistent. The Tonzang landslide (Myanmar test case, **Figure 19**) deeply modified the local morphology, hence the effect of the pre-event PLIA on landslide maps must be interpreted mindfully. In the upper part of the landslide, where the pre-event morphology can be considered at least not completely disrupted, it can be observed that the landslide maps are more clustered on the right side for descending geometry, as opposed to the ascending geometry. This evidence is opposite to the Chile test case, where the borders tend to cluster over lower values of PLIA. Whereas on one hand we consider this an evidence that there were not enough elements to univocally draw the landslide border in those locations of the Tonzang landslide, it is not clear here whether this was caused by little

changes in the backscatter coefficient, or by the PLIA that caused pixel values to show a quite uniform and strong response. The same evidence can be found in **Figure 19D**, where interpreters incorrectly included an area in the scarp (black arrow in **Figure 19D**). Further research is needed to disentangle PLIA effect and magnitude of change of backscatter coefficient in affecting interpreters' ability to map landslides. We underline that this experiment was designed to explore the use of different images to map event landslides, hence a systematic comparison of different images for producing a single map was out of the scope of the study. When it comes to landslide mapping, instead, interpreters should use all the available images to reduce uncertainty and draw the landslide border most coherent with all the information available.
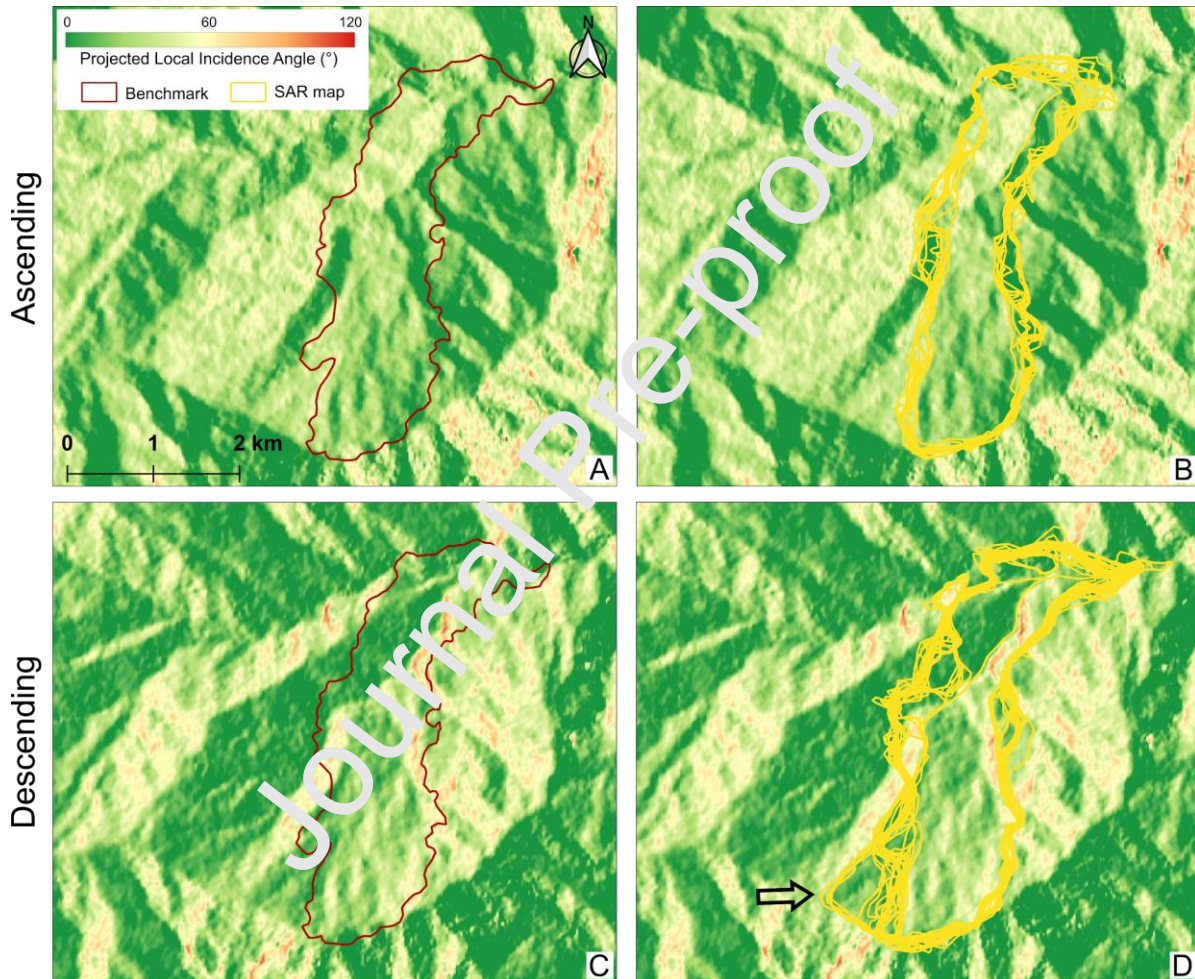
Figure 19 - Maps of the Projected Local Incidence Angle (PLIA) of the Myanmar test case, Ascending (A, B) and Descending (C and D). Benchmark and SAR maps are shown for reference. Figure B shows only maps prepared using ascending images; D shows only maps prepared on descending images. Black arrow indicates a systematic error in the scarp area.

5.2 Evaluation of informative content of SAR backscatter products

Comparison of the mismatch (M_B) in the two test cases reveals that M_B is not unambiguously

attributed to a single factor. In the Villa Santa Lucia landslide, the most influencing factor is the polarisation, with VV data points that cluster in the low mismatch part of the plot (**Figure 13**). In the Tonzang landslide, the most influencing factor is the acquisition geometry (**Figure 16**).

Unlike the Tonzang landslide, the Villa Santa Lucia landslide can be divided in three areas that show large morphological differences, and where the geographical dispersion of mapped landslide borders differs sensibly. Therefore, to further analyse the mismatch data, we have computed the mismatch also within the three different sectors of the Villa Santa Lucia landslide (**Figure 12**). In particular, **Figures 20-22** show plots of the mismatch for each landslide sector, namely scarp (**Figure 20**), body (**Figure 21**), and fan (**Figure 22**). Descriptive statistics on the maps in the three sectors of the landslide are also reported in **Table 2**. Inspection of the figures confirms that the central sector (**Figure 21**) is the one with the least dispersion, i.e., the highest consistency of the maps to the benchmark.

Figure 20 - Distribution of the mismatch between the SAR derived maps of the scarp of the Villa Santa Lucia landslide compared to the benchmark. Data points are ranked by mismatch value (X axis), whereas the corresponding SAR images names are reported on the Y axis, according to the names listed in **Figure 3**, **Figure 4** and **Table A1**. Inset: detail of the scarp of the landslide in the optical post-event image (for details refer to caption of **Figure 1**).

Surprisingly, as opposed to the Villa Santa Lucia landslide, VH images seem to provide more information for an accurate mapping in the Myanmar test case (error is on average ~40% smaller, from ~0.35 to ~0.20, **Figure 19**). Our hypothesis is that VH images are more sensitive than VV images to the surface roughness at the scale of the wavelength (~ 5cm), which may be an indicator of the granulometry of the deposit and/or indicate diffuse erosion of the surface at such scale. The same reason may explain why the VH images were so poorly performing in the fan area of the Villa Santa Lucia landslide (**Figure 22**), where the deposit is mainly constituted by mud.
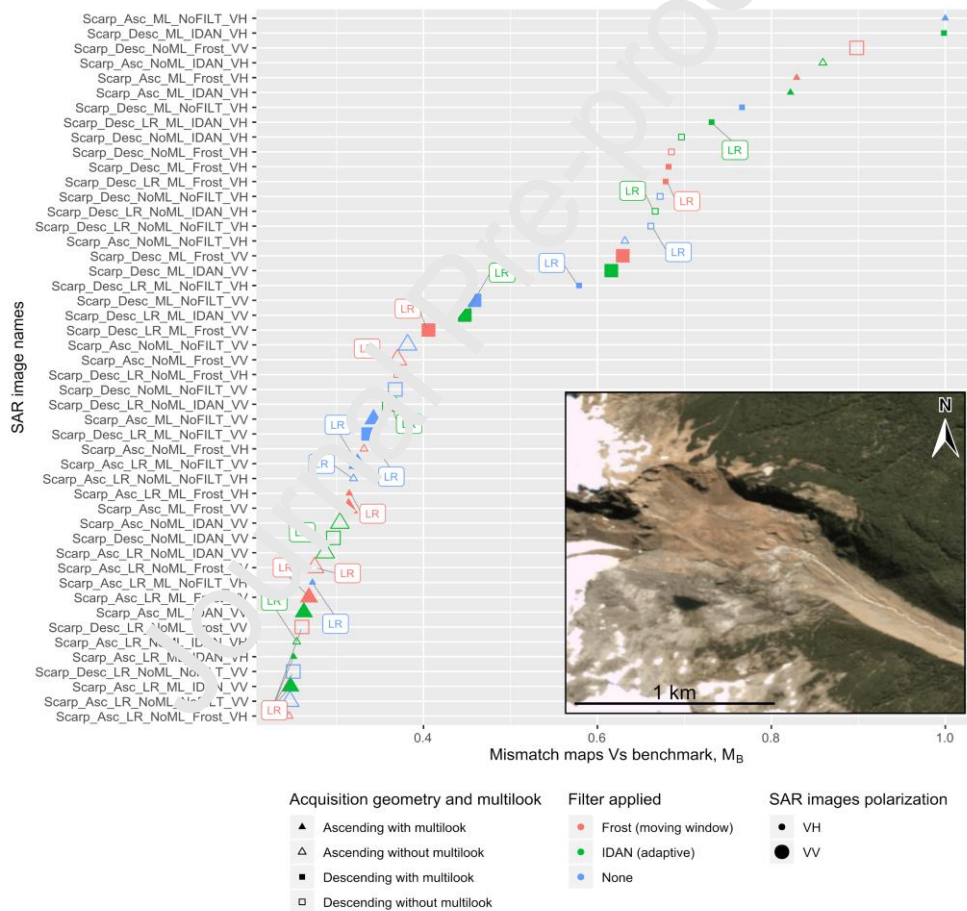

Figure 21 - Distribution of the mismatch between the SAR derived maps of the central part of the Villa Santa Lucia landslide compared to the benchmark. Data points are ranked by mismatch value (X axis), whereas the corresponding SAR images names are reported on the Y axis, according to the names listed in **Figure 3**, **Figure 4** and **Table A1**. Inset: detail of the body of the landslide in the optical post-event image (for details refer to caption of **Figure 1**).

Furthermore, in the Villa Santa Lucia landslide, VH images would allow an internal

characterisation based on evidence of ephemeral channels and diffuse erosion in the central portion of the landslide. Further inspection of **Figures 20-22** reveals that VH images are systematically worse performing in the scarp (**Figure 20**) and fan area (**Figure 22**), whereas in the central part of the landslide (**Figure 21**), the general behaviour is more similar to the Myanmar test case (**Figure 16**). Here acquisition geometry is the most influential factor and descending images are systematically better than ascending, with polarisation playing a minor role. We interpret this behaviour as the result of some similarities in the morphological and radiometric signatures of the Tonzang landslide and the central part of the Villa Santa Lucia landslide, where a mostly regular slope, complete removal of vegetation, absence of snow, presence of deposit material, and favourable aspect direction with respect to the acquisition geometry characterise the landslide.
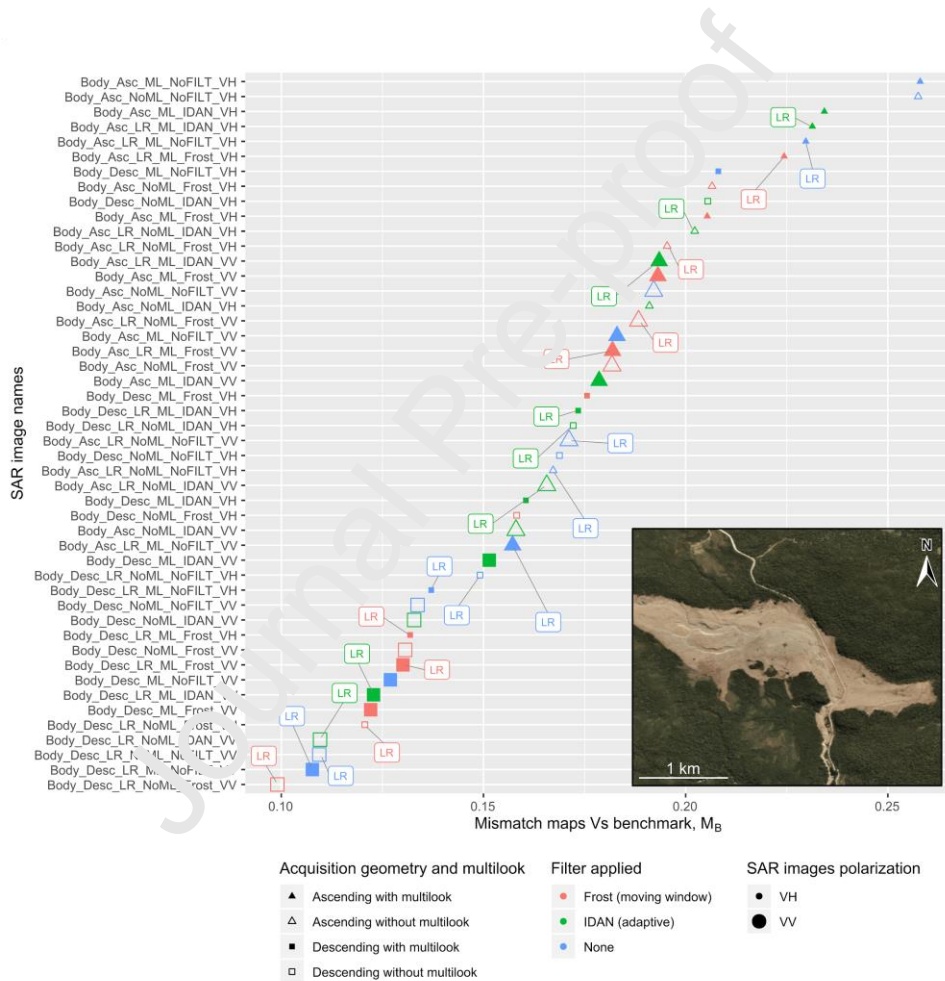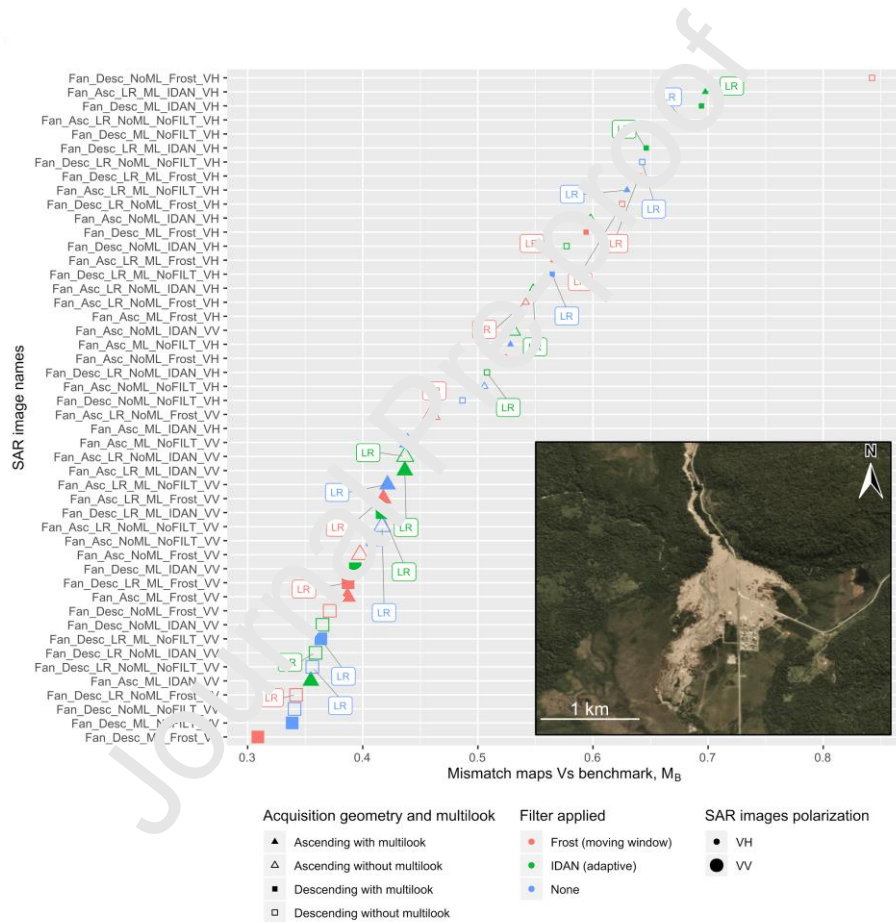

Figure 22 - Distribution of the mismatch between the SAR derived maps of the fan of the Villa Santa Lucia landslide compared to the benchmark. Data points are ranked by mismatch value (X axis), whereas the corresponding SAR images names are reported on the Y axis, according to the names listed in **Figure 3**, **Figure 4** and **Table A1**. Inset: detail of the fan of the landslide in the optical post-event image (for details refer to caption of **Figure 1**).

Plots of M_B also reveal that in both case studies, images of change (LR) are often better performing compared to the corresponding post-event images. In particular, it is evident that LR does not mitigate the effect of polarisation or acquisition geometry, i.e., within groups of M_B data

points pertaining to the same acquisition geometry or polarisation, LR images frequently show the lowest values of mismatch (**Figures 13, 16**). On the other hand, it seems that LR has a higher impact on the mismatch than the application of multilook or filters, which is shown by data points that cluster by LR more than by filters or multilook application. When mapping on LR images, interpreters could not but read a signal of change of the backscatter coefficient, having no possibility to contextualise that signal within the local morphology. For instance, white areas indicate areas where β_0 has increased, which could be due to increase in soil moisture, but also to morphological changes that may lower the PLIA. Despite a good overall performance in highlighting the landslide borders, interpreters are more at ease with images that show absolute values instead of differences, i.e. they prefer having information to filter out (i.e. raw images) than having it done from an algorithm (*Razak et al., 2013*).

Further inspection of mismatch of SAR maps compared to the benchmark also revealed that filters (including multilook) applied to images played a minor role in influencing the mapping results, compared to acquisition geometry and polarisation. This is evident in both case studies (**Figures 13, 16**). Referring to detection, where change is more helpful to identifying and preparing a first mapping (delineation of the landslide border) of the landslide, IDAN is more helpful in emphasizing the border itself, as opposed to Frost filter. On the contrary, the Frost filter helps more in the refined mapping, which is more easily done on post-event images, where also the morphological context is perceived by interpreters. In this case, IDAN introduces a strong generalisation that does not help when interpreters look for details. The effect of generalisation of IDAN filtered images is even stronger when applied to multilook images. Inspection of **Figures 5-8 B,E,H,M**, and **Figures 9-11 B,E,H,M** reveals that images where IDAN was applied to multilook appear blurred. In these cases, the anomaly caused by the landslide is enhanced compared to the surroundings, which helps detection, but details are hidden, hampering accurate mapping. It has to be stated that in this work filters were applied using a single parametrisation. Results here commented refer only to this specific case and cannot be considered general, but need to be specifically investigated.

5.3 Evaluating SAR amplitude derived product for event landslide mapping

In this experiment, interpreters worked on a single landslide without a priori knowledge, the Tonzang landslide, mapping one border for each image. Results showed that, at worst, error was equal to 0.294, whereas the median error was 0.168 (**Table 2**). We acknowledge that the Tonzang landslide has a strong radiometric and morphologic signature, which could make such results case specific and hardly generalizable. Comparison of results for the Villa Santa Lucia landslide reveals that overall M_B values were greater than the Tonzang landslide, despite interpreters having previous knowledge of it. However, if sectors of the Villa Santa Lucia landslide are considered, some similarities emerge in the central part, where it shows a signature and values of M_B (**Table 2**) comparable to the Tonzang landslide, whereas larger mismatch values occurred in the scarp and fan areas. A preliminary hypothesis is that C-band SAR amplitude derived products can be successfully applied where landslides have a radiometric and morphologic signature that causes the radar signal to be sharply different from the surroundings. It may correspond to areas where vegetation has been completely removed, and/or morphology has changed (hence also the PLIA). On the other hand, worse performances are to be expected when, for example, a snowmelt

event takes place (as for the scarp of the Chile test case) between pre- and post-event image acquisition, which introduces noise (*Mondini et al., 2019*). Similar results can be expected when the surface roughness is finer or coarser than the scale of the wavelength (~5 cm), which limits the interaction of the microwaves with the imaged surface, as for the fan of the Chile test case. *Mondini et al., (2019)* stated that in several cases analysed worldwide, they could detect not only single known event landslides, but also landslide events (i.e. populations of event landslides), Myanmar being one of these. Furthermore, their work did not allow for an estimation of a minimum landslide size for detection of event landslides in Sentinel-1 images. We confirm that specific experiments are needed to evaluate such a threshold, both for detection and mapping, which would make clear to what degree of completeness (*Guzzetti et al., 2012*) event inventories can be prepared using SAR amplitude derived products.

Finally, it has to be stated that our results only refer to the specific wavelength (~5 cm) of C-band images at the spatial resolution of 15 m. Other bands would interact with objects at different scales. It is yet not clear whether comparison of different bands would allow for landslide classification (i.e., mud flows Vs debris flows). Also polarisation plays an important role in landslide mapping. It was shown that VH images were generally worse than VV, possibly because VH signal is in general weaker and the borders resulted somewhat fuzzier to interpreters. On the other hand, VH allowed interpreters to identify elements internal to the landslides that could help geomorphologists characterise the landslides internally based on the pattern of the surface roughness at the scale of the wavelength. Further research is needed to gain more experience on different bands, polarimetric composition, possibly with full polarimetric images (*Watanabe et al., 2012; Yamaguchi, 2012*), different environments, different landslide types, different resolutions, filters tuning. Such efforts are needed to better understand to what extent SAR images can effectively support landslide emergency response under severe climatic emergencies, when optical images cannot be available due to cloud cover.

6   Conclusions

In this paper, we explore the use of Sentinel-1 SAR amplitude derived products for event landslide mapping. SAR images included ascending and descending orbits, and a dual-pol acquisition mode (VV and VH). Criteria for interpretation of SAR amplitude derived products to map event landslides, both on post-event images and images of change (LR) of the backscatter coefficient were proposed, and their application led to results comparable to what usually obtained using optical post-event images, even when interpreters have no a priori knowledge of the landslide. This opens to the possibility of using such images for fast emergency response activities. However, results indicate also that interpretation of SAR images can be affected by geometrical distortions. In this experiment, interpreters kept the maps bound to the evidence provided by each single image, limiting as much as possible any learning from other images. In operational contexts, interpreters should reduce the amount of uncertainty by comparing groups of images, including all the factors that were separately examined in this work. We suggest that in landslide event emergency scenarios interpreters analyse and compare multiple images to reduce the sources of ambiguity that may affect mapping accuracy. For expert interpretation in emergency scenarios, we suggest that images of change be used for landslide detection and preliminary mapping. Then, interpreters should refine the preliminary mapping by comparing

pre- and post-event images, from different (i) orbits, to reduce geometric issues due to the PLIA, shadowing and layover, and (ii) polarisations to make inferences about the surface roughness. Interestingly, interpretation mitigated the speckling-like effects, which suggests that use of different filters is weakly influential on mapping results, with some advantage offered by adaptive filters (IDAN) for detection. Finally, it must be stated that, due to the geographically limited test cases, this work has to be considered a preliminary study which cannot support the definition of worldwide valid operational guidelines for event landslide inventory making. Nevertheless, we maintain that our findings allowed collecting first insights on which images characteristics of SAR amplitude derived products maximise the evidence of event landslides of similar size and type as the ones analysed in the two test cases. Building on such findings, future works may explore potential and limitations for preparing event landslide inventories.

7 Declaration of competing interest

The authors declare that they have no known competing financial interests or personal relationships that could have appeared to influence the work reported in this paper.

8 Acknowledgements

9 Authors' contribution

MS designed the experiment, performed the images processing, interpreted the images, analysed the data and wrote the paper. MC interpreted the images, and wrote the paper; FF interpreted the images, and wrote the paper; PR interpreted the images, and wrote the paper, ACM designed the experiment, performed the images pre-processing, and wrote the paper.

10 References

Adriano, B., Yokoya, N., Miura, H., Matsuoka, M., Koshimura, S., 2020. A Semiautomatic Pixel-Object Method for Detecting Landslides Using Multitemporal ALOS-2 Intensity Images. Remote Sens. 12, 561. https://doi.org/10.3390/rs12030561

Alvioli, M., Mondini, A.C., Fiorucci, F., Cardinali, M., Marchesini, I., 2018. Topography-driven satellite imagery analysis for landslide mapping. Geomat. Nat. Hazards Risk 9, 544–567. https://doi.org/10.1080/19475705.2018.1458050

Ardizzone, F., Basile, G., Cardinali, M., Casagli, N., Del Conte, S., Del Ventisette, C., Fiorucci, F., Garfagnoli, F., Gigli, G., Guzzetti, F., Iovine, G., Mondini, A.C., Moretti, S., Panebianco, M., Raspini, F., Reichenbach, P., Rossi, M., Tanteri, L., Terranova, O., 2012. Landslide inventory

map for the Briga and the Giampilieri catchments, NE Sicily, Italy. J. Maps 8, 176–180. https://doi.org/10.1080/17445647.2012.694271

Ardizzone, F., Cardinali, M., Carrara, A., Guzzetti, F., Reichenbach, P., 2002. Impact of mapping errors on the reliability of landslide hazard maps. Nat. Hazards Earth Syst. Sci. 2, 3–14. https://doi.org/10.5194/nhess-2-3-2002

Bucci, F., Cardinali, M., Guzzetti, F., 2013. Structural geomorphology, active faulting and slope deformations in the epicentre area of the MW 7.0, 1857, Southern Italy earthquake. Phys. Chem. Earth Parts ABC 63, 12–24. https://doi.org/10.1016/j.pce.2013.04.005

Carrara, A., 1993. Uncertainty in Evaluating Landslide Hazard and Risk, in: Nemec, J., Nigg, J.M., Siccardi, F. (Eds.), Prediction and Perception of Natural Hazards: Proceedings Symposium, 22–26 October 1990, Perugia, Italy, Advances in Natural and Technological Hazards Research. Springer Netherlands, Dordrecht, pp. 101–109. https://doi.org/10.1007/978-94-015-8190-5_12

Chorowicz, J., Scanvic, J.Y., Rouzeau, O., Cuervo, G.V., 1998. Observation of recent and active landslides from SAR ERS-1 and JERS-1 imagery using a stereo-simulation approach: Example of the Chicamocha valley in Colombia. Int. J. Remote Sens. 19, 3187–3196. https://doi.org/10.1080/014311698214253

Colesanti, C., Wasowski, J., 2006. Investigating landslides with space-borne Synthetic Aperture Radar (SAR) interferometry. Eng. Geol. 88, 173–199. https://doi.org/10.1016/j.enggeo.2006.09.013

Duhart, P., Sepúlveda, V., Garrido, N., Mella, M., Quiroz, D., Fernández, J., Moreno, H., Hermosilla, G., 2019. The Santa Lucía landslide disaster, Chaitén Chile: origin and effects 8.

Earth Resources Observation And Science (EROS) Center, 2017. Shuttle Radar Topography Mission (SRTM) 1 Arc-Second Global. https://doi.org/10.5066/F7PR7TFT

El-Darymli, K., McGuire, P., Gill, E., Power, D., Moloney, C., 2014. Understanding the significance of radiometric calibration for synthetic aperture radar imagery, in: 2014 IEEE 27th Canadian Conference on Electrical and Computer Engineering (CCECE). Presented at the 2014 IEEE 27th Canadian Conference on Electrical and Computer Engineering (CCECE), pp. 1–6. https://doi.org/10.1109/CCECE.2014.6901104

Esposito, G., Marchesini, I., Mondini, A.C., Reichenbach, P., Rossi, M., Sterlacchini, S., 2020. A spaceborne SAR-based procedure to support the detection of landslides. Nat. Hazards Earth Syst. Sci. 20, 2379–2395. https://doi.org/10.5194/nhess-20-2379-2020

Fiorucci, F., Cardinali, M., Carlà, R., Rossi, M., Mondini, A.C., Santurri, L., Ardizzone, F., Guzzetti, F., 2011. Seasonal landslide mapping and estimation of landslide mobilization rates using aerial and satellite images. Geomorphology 129, 59–70. https://doi.org/10.1016/j.geomorph.2011.01.013

Fiorucci, F., Giordan, D., Santangelo, M., Dutto, F., Rossi, M., Guzzetti, F., 2018. Criteria for the optimal selection of remote sensing optical images to map event landslides 405–417. https://doi.org/10.5194/nhess-18-405-2018

Francis, P., 1993. Volcanoes: a planetary perspective. Clarendon Press ; Oxford University Press, Oxford; New York.

Freeman, A., 1992. SAR calibration: an overview. IEEE Trans. Geosci. Remote Sens. 30, 1107–1121. https://doi.org/10.1109/36.193786

Frost, V.S., Stiles, J.A., Shanmugan, K.S., Holtzman, J.C., 1982. A Model for Radar Images and Its Application to Adaptive Digital Filtering of Multiplicative Noise. IEEE Trans. Pattern Anal. Mach. Intell. PAMI-4, 157–166. https://doi.org/10.1109/TPAMI.1982.4767223

Furuta, R., Tomiyama, N., 2008. A Study of Detection of Landslide Disasters due to the Pakistan Earthquake using ALOS data.

Ge, P., Gokon, H., Meguro, K., Koshimura, S., 2019. Study on the Intensity and Coherence Information of High-Resolution ALOS-2 SAR Images for Rapid Massive Landslide Mapping at a Pixel Level. Remote Sens. 11, 2808. https://doi.org/10.3390/rs11232808

GRASS Development Team, 2017. Geographic Resources Analysis Support System (GRASS GIS) Software, Version 7.2.

Gutiérrez, F., Soldati, M., 2018. Landforms, in: Bobrowsky, P.T., Marker, B. (Eds.), Encyclopedia of Engineering Geology. Springer International Publishing, Cham, pp. 565–579. https://doi.org/10.1007/978-3-319-73568-9_181

Guzzetti, F., Mondini, A.C., Cardinali, M., Fiorucci, F., Santangelo, M., Chang, K.-T., 2012. Landslide inventory maps: New tools for an old problem. Earth-Sci. Rev. 112, 42–66. https://doi.org/10.1016/j.earscirev.2012.02.001

Jaboyedoff, M., Michoud, C., Derron, M.-H., Voumard, jérémie, Leibundgut, G., Sudmeier-Rieux, K., Nadim, F., Leroi, E., 2016. Human-Induced Landslides: Toward the analysis of anthropogenic changes of the slope environment. pp. 217–232. https://doi.org/10.1201/b21520-20

Konishi, T., Suga, Y., 2018a. Landslide detection using COSMO-SkyMed images: a case study of a landslide event on Kii Peninsula, Japan. Eur. J. Remote Sens. 51, 205–221. https://doi.org/10.1080/22797254.2017.1418185

Konishi, T., Suga, Y., 2018b. Landslide detection using polarimetric ALOS-2/PALSAR-2 data: a case study of 2016 Kumamoto earthquake in Japan, in: Active and Passive Microwave Remote Sensing for Environmental Monitoring II. Presented at the Active and Passive Microwave Remote Sensing for Environmental Monitoring II, International Society for Optics and Photonics, p. 107880P. https://doi.org/10.1117/12.2324030

Lee, J.S., Jurkevich, L., Dewaele, P., Wambacq, P., Oosterlinck, A., 1994. Speckle filtering of synthetic aperture radar images: A review. Remote Sens. Rev. 8, 313–340. https://doi.org/10.1080/02757259409532206

Mondini, A., Santangelo, M., Rocchetti, M., Rossetto, E., Manconi, A., Monserrat, O., 2019. Sentinel-1 SAR Amplitude Imagery for Rapid Landslide Detection. Remote Sens. 11, 760. https://doi.org/10.3390/rs11070760

Mondini, A.C., 2017. Measures of Spatial Autocorrelation Changes in Multitemporal SAR Images for Event Landslides Detection. Remote Sens. 9, 554. https://doi.org/10.3390/rs9060554

Mondini, A.C., Chang, K., Rossi, M., Marchesini, I., Guzzetti, F., 2012. Semi-automatic recognition and mapping of event-induced landslides by exploiting multispectral satellite images and DEM in a Bayesian framework, in: Entekhabi, D., Honda, Y., Sawada, H., Shi, J., Oki, T. (Eds.), p. 852415. https://doi.org/10.1117/12.977432

Mondini, A. C., Guzzetti, F., Chang, K.-T., Monserrat, O., Martha, T. R., and Manconi, A.: Landslide failures detection and mapping using Synthetic Aperture Radar: Past, present and future, Earth-Sci. Rev., 216, 103574, https://doi.org/10.1016/j.earscirev.2021.103574, 2021.

Niculiţă, M., Mărgărint, M.C., Santangelo, M., 2016. Archaeological evidence for Holocene landslide activity in the Eastern Carpathian lowland. Quat. Int. http://dx.doi.org/10.1016/j.quaint.2015.12.048

Oliver, C., Quegan, S., 2004. Understanding Synthetic Aperture Radar Images. SciTech Publishing, Inc., Raleigh, NC 27613.

Plank, S., Twele, A., Martinis, S., 2016. Landslide Mapping in Vegetated Areas Using Change Detection Based on Optical and Polarimetric SAR Data. Remote Sens. 8, 307. https://doi.org/10.3390/rs8040307

Ray, R.G., 1960. Aerial photographs in geologic interpretation and mapping (Professional Paper No. 373), Geological Survey Professional Paper. USGS, SPokane, Washington.

Razak, K.A., Santangelo, M., Van Westen, C.J., Straatsma, M.W., de Jong, S.M., 2013. Generating an optimal DTM from airborne laser scanning data for landslide mapping in a tropical forest environment. Geomorphology 190, 112–125. https://doi.org/10.1016/j.geomorph.2013.02.021

Santangelo, M., Alvioli, M., Baldo, M., Cardinali, M., Giordan, D., Guzzetti, F., Marchesini, I., Reichenbach, P., 2019. Brief communication: Remotely piloted aircraft systems for rapid emergency response: road exposure to rockfall in Villanova di Accumoli (central Italy). Nat. Hazards Earth Syst. Sci. 19, 325–335. https://doi.org/10.5194/nhess-19-325-2019

Santangelo, M., Cardinali, M., Rossi, M., Mondini, A.C., Guzzetti, F., 2010. Remote landslide mapping using a laser rangefinder binocular and GPS. Nat. Hazards Earth Syst. Sci. 10, 2539–2546. https://doi.org/10.5194/nhess-10-2539-2010

Santangelo, M., Gioia, D., Cardinali, M., Guzzetti, F., Schiattarella, M., 2014. Landslide inventory map of the upper Sinni River valley, Southern Italy. J. Maps 0, 1–10. https://doi.org/10.1080/17445647.2014.949313

Santangelo, M., Marchesini, I., Bucci, F., Cardinali, M., Fiorucci, F., Guzzetti, F., 2015. An approach to reduce mapping errors in the production of landslide inventory maps. Nat. Hazards Earth Syst. Sci. Discuss. 3, 4189–4229. https://doi.org/10.5194/nhessd-3-4189-2015

Singhroy, V., 1995. Sar integrated techniques for geohazard assessment. Adv. Space Res., Natural Hazards: Monitoring and Assessment Using Remote Sensing Technique 15, 67–78. https://doi.org/10.1016/0273-1177(95)00076-Q

Singhroy, V., Mattar, K.E., Gray, A.L., 1998. Landslide characterisation in Canada using interferometric SAR and combined SAR and TM images. Adv. Space Res., Remote Sensing: Inversion Problems and Natural Hazards 21, 465–476. https://doi.org/10.1016/S0273-1177(97)00882-X

Small, D., Schubert, A., 2008. Guide to ASAR Geocoding (No. 1.01), RSL-ASAR-GC-AD. University of Zurich.

Suga, Y., Konishi, T., 2012. Landslide detection using very high-resolution satellite imageries, in: Land Surface Remote Sensing. Presented at the Land Surface Remote Sensing, International Society for Optics and Photonics, p. 85240B. https://doi.org/10.1117/12.976033

The World Bank, 2015. Myanmar : Post-disaster needs assessment of floods and landslides : July - September 2015 (No. 103531), The World Bank.

Uemoto, J., Moriyama, T., Nadai, A., Kojima, S., Umehara, T., 2019. Landslide detection based on height and amplitude differences using pre- and post-event airborne X-band SAR data. Nat. Hazards 95, 485–503. https://doi.org/10.1007/s11069-018-3492-8

van Zuidam, R.A., 1986. Aerial photo-interpretation in terrain analysis and geomorphologic mapping. Smits, Publishers, The Hague.

Vargas Cuervo, G., 1997. Evaluacion de Imagenes de Satelite SAR ERS-1 Y Spot-Landsat EN la Cartografia de Movimientos EN Masa 405, 109.

Vasile, G., Trouve, E., Jong-Sen Lee, Buzuloiu, V., 2006. Intensity-driven adaptive-neighborhood technique for polarimetric and interferometric SAR parameters estimation. IEEE Trans. Geosci. Remote Sens. 44, 1609–1621. https://doi.org/10.1109/TGRS.2005.864142

Watanabe, M., Yonezawa, C., Iisaka, J., Sato, M., 2012. ALOS/PALSAR full polarimetric observations of the Iwate–Miyagi Nairiku earthquake of 2008. Int. J. Remote Sens. 33, 1234–1245. https://doi.org/10.1080/01431161.2011.554453

Yamaguchi, Y., 2012. Disaster Monitoring by Fully Polarimetric SAR Data Acquired With ALOS-PALSAR. Proc. IEEE 100, 2851–2860. https://doi.org/10.1109/JPROC.2012.2195469

Zaw, K., Swe, W., Barber, A.J., Crow, M.J., Nwe, Y.Y., 2017. Introduction to the geology of Myanmar, in: Barber, A.J., Khin, Z., Crow, M.J. (Eds.), Myanmar: Geology, Resources and Tectonics. Geological Society, London, pp. 1–17.

11 Web references

Copernicus Open Access Hub, 2021. https://scihub.copernicus.eu/dhus/#/home (accessed 18 October 2021).

STEP - Scientific Toolbox Exploitation Platform, 2021. http://step.esa.int/main/ (accessed 18 October 2021).

The European Space Agency, 2021a. Sentinel-1 product specifications. https://sentinel.esa.int/web/sentinel/document-library/content/-/article/sentinel-1-product-specification (accessed 18 October 2021).

The European Space Agency, 2021b. Sentinel-1 SAR Technical Guide. https://sentinel.esa.int/web/sentinel/technical-guides/sentinel-1-sar (accessed 18 October 2021).

The European Space Agency, 2021c. Sentinel-1 Document Library. https://sentinel.esa.int/web/sentinel/user-guides/sentinel-1-sar/document-library/-/asset_publisher/1dO7RF5fJMbd/content/thermal-denoising-of-products-generated-by-the-sentinel-1-ipf (accessed 18 October 2021).

The European Space Agency, 2021d. Level-1 Radiometric Calibration. https://sentinel.esa.int/web/sentinel/radiometric-calibration-of-level-1-products (accessed 18 October 2021).

12 Appendix

Table A1 - Names and characteristics of the images used in this paper. The first column indicates the ascending (Asc) or descending (Desc) orbit; the column Time Step reports whether the images are pre-event (Pre) or post-event (Post); the column Pol indicates the polarisation (VV or VH); the fourth column (ML) reports whether for that image Multilook has been performed; in the fifth column (Filt) it is reported "No" for non-filtered images, and "Frost" or "IDAN" to indicate the filter used; the column LR indicates whether the image is an image of change (Log-Ratio). In the column "Image name" it is reported the name assigned to each image, according to **Figure 3** and **Figure 4**. In the last two columns, where applicable, it is reported the order in which the images were shown to interpreters. Ranking is ordered from lowest to highest for Chile, whereas for Myanmar it is possible to read the rank number compared to the images of Chile. Order of Myanmar images was decided based on results of comparison between SAR images based maps and the benchmark, so that images with higher mapping error were interpreted first. See text for further explanation.

Orbit	Time step	Pol	ML	FILT	LR	Image name	Order [#], Chile	Order [#], Myanmar
Asc	Pre	VV	Yes	No	No	Asc_Pre_ML_NoFILT_VV	1	18
Asc	Post	VV	Yes	No	No	Asc_ML_NoFILT_VV	1	18
Asc	Post	VV	Yes	No	Yes	Asc_LR_ML_NoFILT_VV	2	24
Asc	Pre	VH	Yes	No	No	Asc_Pre_ML_NoFILT_VH	3	NA
Asc	Post	VH	Yes	No	No	Asc_ML_NoFILT_VH	3	NA
Asc	Post	VH	Yes	No	Yes	Asc_LR_ML_NoFILT_VH	4	NA
Asc	Pre	VV	Yes	IDAN	No	Asc_Pre_ML_IDAN_VV	5	26
Asc	Post	VV	Yes	IDAN	No	Asc_ML_IDAN_VV	5	26
Asc	Post	VV	Yes	IDAN	Yes	Asc_LR_ML_IDAN_VV	6	15
Asc	Pre	VH	Yes	IDAN	No	Asc_Pre_ML_IDAN_VH	7	NA
Asc	Post	VH	Yes	IDAN	No	Asc_ML_IDAN_VH	7	NA
Asc	Post	VH	Yes	IDAN	Yes	Asc_LR_ML_IDAN_VH	8	NA
Asc	Pre	VV	Yes	Frost	No	Asc_Pre_ML_Frost_VV	9	20
Asc	Post	VV	Yes	Frost	No	Asc_ML_Frost_VV	9	20

Asc	Post	VV	Yes	Frost	Yes	*Asc_LR_ML_Frost_VV*	10	21
Asc	Pre	VH	Yes	Frost	No	*Asc_Pre_ML_Frost_VH*	11	NA
Asc	Post	VH	Yes	Frost	No	*Asc_ML_Frost_VH*	11	NA
Asc	Post	VH	Yes	Frost	Yes	*Asc_LR_ML_Frost_VH*	12	NA
Asc	Pre	VV	No	No	No	*Asc_Pre_NoML_NoFILT_VV*	13	16
Asc	Post	VV	No	No	No	*Asc_NoML_NoFILT_VV*	13	16
Asc	Post	VV	No	No	Yes	*Asc_LR_NoML_NoFILT_VV*	14	25
Asc	Pre	VH	No	No	No	*Asc_Pre_NoML_NoFILT_VH*	15	NA
Asc	Post	VH	No	No	No	*Asc_NoML_NoFILT_VH*	15	NA
Asc	Post	VH	No	No	Yes	*Asc_LR_NoML_NoFILT_VH*	16	NA
Asc	Pre	VV	No	IDAN	No	*Asc_Pre_NoML_IDAN_VV*	17	17
Asc	Post	VV	No	IDAN	No	*Asc_NoML_IDAN_VV*	17	17
Asc	Post	VV	No	IDAN	Yes	*Asc_LR_NoML_IDAN_VV*	18	23
Asc	Pre	VH	No	IDAN	No	*Asc_Pre_NoML_IDAN_VH*	19	NA
Asc	Post	VH	No	IDAN	No	*Asc_NoML_IDAN_VH*	19	NA
Asc	Post	VH	No	IDAN	Yes	*Asc_LR_NoML_IDAN_VH*	20	NA
Asc	Pre	VV	No	Frost	No	*Asc_Pre_NoML_Frost_VV*	21	22
Asc	Post	VV	No	Frost	No	*Asc_NoML_Frost_VV*	21	22
Asc	Post	VV	No	Frost	Yes	*Asc_LR_NoML_Frost_VV*	22	14
Asc	Pre	VH	No	Frost	No	*Asc_Pre_NoML_Frost_VH*	23	NA
Asc	Post	VH	No	Frost	No	*Asc_NoML_Frost_VH*	23	NA
Asc	Post	VH	No	Frost	Yes	*Asc_LR_NoML_Frost_VH*	24	NA
Desc	Pre	VV	Yes	No	No	*Desc_Pre_ML_NoFILT_VV*	25	30
Desc	Post	VV	Yes	No	No	*Desc_ML_NoFILT_VV*	25	30
Desc	Post	VV	Yes	No	Yes	*Desc_LR_ML_NoFILT_VV*	26	33
Desc	Pre	VH	Yes	No	No	*Desc_Pre_ML_NoFILT_VH*	27	2
Desc	Post	VH	Yes	No	No	*Desc_ML_NoFILT_VH*	27	2
Desc	Post	VH	Yes	No	Yes	*Desc_LR_ML_NoFILT_VH*	28	10
Desc	Pre	VV	Yes	IDAN	No	*Desc_Pre_ML_IDAN_VV*	29	19
Desc	Post	VV	Yes	IDAN	No	*Desc_ML_IDAN_VV*	29	19
Desc	Post	VV	Yes	IDAN	Yes	*Desc_LR_ML_IDAN_VV*	30	27
Desc	Pre	VH	Yes	IDAN	No	*Desc_Pre_ML_IDAN_VH*	31	3
Desc	Post	VH	Yes	IDAN	No	*Desc_ML_IDAN_VH*	31	3
Desc	Post	VH	Yes	IDAN	Yes	*Desc_LR_ML_IDAN_VH*	32	4
Desc	Pre	VV	Yes	Frost	No	*Desc_Pre_ML_Frost_VV*	33	29
Desc	Post	VV	Yes	Frost	No	*Desc_ML_Frost_VV*	33	29
Desc	Post	VV	Yes	Frost	Yes	*Desc_LR_ML_Frost_VV*	34	28
Desc	Pre	VH	Yes	Frost	No	*Desc_Pre_ML_Frost_VH*	35	6
Desc	Post	VH	Yes	Frost	No	*Desc_ML_Frost_VH*	35	6
Desc	Post	VH	Yes	Frost	Yes	*Desc_LR_ML_Frost_VH*	36	9
Desc	Pre	VV	No	No	No	*Desc_Pre_NoML_NoFILT_VV*	37	31
Desc	Post	VV	No	No	No	*Desc_NoML_NoFILT_VV*	37	31
Desc	Post	VV	No	No	Yes	*Desc_LR_NoML_NoFILT_VV*	38	35
Desc	Pre	VH	No	No	No	*Desc_Pre_NoML_NoFILT_VH*	39	11
Desc	Post	VH	No	No	No	*Desc_NoML_NoFILT_VH*	39	11
Desc	Post	VH	No	No	Yes	*Desc_LR_NoML_NoFILT_VH*	40	7
Desc	Pre	VV	No	IDAN	No	*Desc_Pre_NoML_IDAN_VV*	41	32
Desc	Post	VV	No	IDAN	No	*Desc_NoML_IDAN_VV*	41	32
Desc	Post	VV	No	IDAN	Yes	*Desc_LR_NoML_IDAN_VV*	42	34
Desc	Pre	VH	No	IDAN	No	*Desc_Pre_NoML_IDAN_VH*	43	5
Desc	Post	VH	No	IDAN	No	*Desc_NoML_IDAN_VH*	43	5
Desc	Post	VH	No	IDAN	Yes	*Desc_LR_NoML_IDAN_VH*	44	8
Desc	Pre	VV	No	Frost	No	*Desc_Pre_NoML_Frost_VV*	45	13
Desc	Post	VV	No	Frost	No	*Desc_NoML_Frost_VV*	45	13
Desc	Post	VV	No	Frost	Yes	*Desc_LR_NoML_Frost_VV*	46	36
Desc	Pre	VH	No	Frost	No	*Desc_Pre_NoML_Frost_VH*	47	1
Desc	Post	VH	No	Frost	No	*Desc_NoML_Frost_VH*	47	1
Desc	Post	VH	No	Frost	Yes	*Desc_LR_NoML_Frost_VH*	48	12

Highlights

- Explored the use of C-band SAR amplitude images to map event landslides
- Interpretation criteria of brightness coefficient (β_0) post-event and change images
- Geometries, polarisation and local incidence angle mostly influence mapping results
- Images of change should be used for preliminary mapping and post-event for refining
- Results open to efficient event landslide mapping in emergency scenarios